DIPLOMARBEIT

The role of contaminations in the interaction of highly charged ions with 2D materials

zur Erlangung des akademischen Grades

Diplom-Ingenieurin

im Rahmen des Studiums

Technische Physik

eingereicht von

Anna NIGGAS
Matrikelnummer 01427256

Ausgeführt am
Institut für Angewandte Physik
der Fakultät für Physik
der Technischen Universität Wien

unter der Anleitung von
Univ.Ass. Dr. Richard A. WILHELM,
Dipl.Ing. Janine SCHWESTKA
und
Univ.Prof. Dr. Friedrich AUMAYR

Wien, 15. Oktober 2019

Anna Niggas	Friedrich Aumayr	Richard A. Wilhelm

Abstract

Contaminations on two dimensional materials can influence electronic, optical and mechanical material properties or even dominate them. We perform ion beam spectroscopy with highly charged ions as projectiles transmitted through free-standing 2D materials to study fundamental charge exchange processes between the ion and the sample.

We employ an electron beam ion source to produce ions with charge states in the range of Xe^{1+} to Xe^{44+} which can be extracted from the source with tunable kinetic energies (1-400 keV). The projectiles are transmitted through the free-standing 2D materials and capture as well as stabilise electrons due to the interaction. We measure the exit charge state of the primary ions after transmission in coincidence with emitted electrons from the sample due to the ion impact. Additionally, we record the time of flight of Xe ions from the target position to the detector to gain information on their energy loss in the sample.

Both, exit charge state and energy loss critically depend on the sample thickness and will be influenced by contaminations on either side of the two dimensional materials. To aim at reaching a clean 2D sample so that the projectile exit charge state and the measured electron emission yields are dominated by the 2D layer rather than by contaminations (e.g. water molecules, hydrocarbons, PMMA) I try different ways to clean our samples: employing a heating wire as well as a laser (445 nm, 6 W) creates clean(er) samples and shifts the exit charge state to higher and the time of flight to lower values. I show that I achieve a cleaned target state which I at least cannot further improve with the methods at hand.

Measurements using cleaned single, bi- and trilayer graphene samples are discussed in the end of this thesis with respect to charge exchange in dependence of the number of graphene layers, scattering angles and neutralisation times of highly charged Xe ions transmitted through these samples.

Kurzfassung

Kontaminationen auf zweidimensionalen Materialien können elektronische, optische oder mechanische Eigenschaften des Materials beeinflussen oder sogar dominieren. Wir nutzen hochgeladene Xenonionen als Projektile für Ionenspektroskopie, die durch freistehende 2D-Materialien transmittiert werden. Dabei studieren wir fundamentale Ladungsaustauschprozesse zwischen dem Ion und der Probe.

Wir verwenden eine Elektronenstrahlionenquelle (electron beam ion source, EBIS), um Ionen mit Ladungszuständen im Bereich Xe^{1+}-Xe^{44+} zu produzieren, die mit einstellbarer kinetischer Energie (1-400 keV) aus der Ionenquelle extrahiert werden. Die Projektile werden dann durch freistehende 2D-Materialien transmittiert und fangen sowie stabilisieren bei der Wechselwirkung Elektronen. Wir messen den Austrittsladungszustand der Primärionen nach Transmission durch die Probe in Koinzidenz mit Elektronen, die bei der Wechselwirkung vom Material emittiert werden. Zusätzlich nehmen wir die Flugzeit der Xenonionen von der Position der Probe bis zu einem Detektor auf, um Informationen über deren Energieverlust im Material zu erlangen.

Sowohl der Austrittsladungszustand als auch der Energieverlust hängen kritisch von der Materialdicke ab und werden von Kontaminationen auf beiden Seiten des 2D-Materials beeinflusst. Um sicherzugehen, dass unsere zweidimensionalen Proben sauber sind und dass der Ausgangsladungszustand des Projektils sowie die detektierte Elektronenemissionsausbeute vom 2D-Material dominiert sind und nicht von Kontaminationen (wie z.B. Wasser, Kohlenwasserstoffe, PMMA), versuche ich mit verschiedenen Möglichkeiten unsere Proben zu reinigen: die Verwendung von einem Heizdraht und von einem Laser (445 nm, 6 W) verlagert den Ausgangsladungszustand zu höheren und die Flugzeit zu kleineren Werten und erzeugt somit saubere(re) Proben. Ich zeige, dass ich gut gereinigte Probenzustände erreiche, die zumindest mithilfe unserer Möglichkeiten nicht mehr verbessert werden können.

Messungen mit gereinigten Proben von Mono-, Bi- und Trilagengraphen werden am Ende dieser Arbeit in Bezug auf Streuwinkel, Ladungsaustausch und Neutralisationszeiten von hochgeladenen Xenonionen jeweils in Abhängigkeit der Graphenlagen diskutiert.

Research experience

Publications in scientific journals

J. Schwestka, D. Melinc, R. Heller, **A. Niggas**, L. Leonhartsberger, H. Winter, S. Facsko, F. Aumayr and R.A. Wilhelm: A versatile ion beam spectrometer for studies of ion interaction with 2D materials, *Review of Scientific Instruments*, vol. 89, p. 085101, 2018.

J. Schwestka, **A. Niggas**, S. Creutzburg, R. Kozubek, R. Heller, M. Schleberger, R.A. Wilhelm and F. Aumayr: Charge-Exchange-Driven Low-Energy Electron Splash Induced by Heavy Ion Impact on Condensed Matter, *Journal of Physical Chemistry Letters*, vol. 2019, p. 4805, 2019.

Contributions to international conferences

J. Schwestka, S. Creutzburg, **A.Niggas**, R. Heller, R. Kozubek, L. Madauss, M. Tripathi, H. Inani, S. Facsko, M. Schleberger, J. Kotakoski, R.A. Wilhelm and F. Aumayr: *Ion-induced electron emission from 2D materials*, Poster: 10th workshop "Towards Reality in Nanoscale Materiasls" (TRNM X), Levi/Finland, 2019

R.A. Wilhelm, P.L. Grande, S. Creutzburg, J. Schwestka, **A. Niggas** and F. Aumayr: *Unraveling energy loss processes of ions in 2D materials - the role of Interatomic Coulombic Decay, the charge state, and charge exchange in nuclear and electronic stopping*, Poster: 13th European Conference on Atoms, Molecules and Photons (ECAMP 13), Florence/Italy 2019

S. Creutzburg, J. Schwestka, H. Inani, M. Tripathi, R. Heller, N. Klingner, **A. Niggas**, T. Lehnert, R. Leiter, R. Kozubek, S. Facsko, U. Kaiser, J. Kotakoski, M. Schleberger, F. Aumayr and R.A. Wilhelm: *Energy deposition of heavy ions in freestanding 2D materials*, Poster: 13th European Conference on Atoms, Molecules and Photons (ECAMP 13), Florence/Italy 2019

R.A. Wilhelm, S. Creutzburg, J. Schwestka, **A. Niggas** and F. Aumayr: Unraveling energy loss processes of ions in 2D materials, Poster: 1st symposium on Electron, Photon and Ion Collisions on Molecular and Atomic Nanostructures (1. EPIC MAN), Caen/France 2019

S. Creutzburg, J. Schwestka, H. Inani, M.K. Tripathi, P.L. Grande, R. Heller, N. Klingner, **A. Niggas**, R. Kozubek, L. Madauß, S. Facsko, J. Kotakoski, M. Schleberger, F. Aumayr and R.A. Wilhelm: *Energy deposition of highly charged ions transmitted through single layer MoS2*, Poster: 1st symposium on Electron, Photon and Ion Collisions on Molecular and Atomic Nanostructures (1. EPIC MAN), Caen/France 2019

A. Niggas, J. Schwestka, S. Lohmann, S. Creutzburg, D. Primetzhofer, R.A. Wilhelm and F. Aumayr: *Electron emission due to ion transmission through freestanding single layer graphene*, Poster: 1st symposium on Electron, Photon and Ion Collisions on Molecular and Atomic Nanostructures (1. EPIC MAN), Caen/France 2019

J. Schwestka, **A. Niggas**, S. Creutzburg, R. Kozubek, L. Madauß, R. Heller, M. Schleberger, S. Facsko, R.A. Wilhelm and F. Aumayr: *Highly charged ion impact on graphene leading to the emission of low energy electrons*, Poster: 31st International Conference on Photonic, Electronic and Atomic Collisions (ICPEAC 2019), Deauville/France 2019

S. Creutzburg, J. Schwestka, H. Inani, M.K. Tripathi, P.L. Grande, R. Heller, N. Klingner, **A. Niggas**, R. Kozubek, L. Madauß, S. Facsko, J. Kotakoski, M. Schleberger, F. Aumayr and R.A. Wilhelm: *Energy deposition of highly charged ions transmitted through single layer MoS2*, Poster: 31st International Conference on Photonic, Electronic and Atomic Collisions (ICPEAC 2019), Deauville/France 2019

A. Niggas, J. Schwestka, S. Creutzburg, F. Aumayr and R.A. Wilhelm: *The role of contaminations in the interaction of highly charged ions with 2D materials*, Poster: 31st International Conference on Photonic, Electronic and Atomic Collisions (ICPEAC 2019), Deauville/France 2019 - **Best Poster Prize**

Research stays

Uppsala Universitet, Department of Physics and Astronomy, Assoc. Prof. Daniel Primetzhofer: *Transmission of medium energy ions through single layer graphene. A time of flight approach to measure electron energies.*, Uppsala/Sweden 08/08/2018 - 19/09/2018

Uppsala Universitet, Department of Physics and Astronomy, Assoc. Prof. Daniel Primetzhofer: *Electron emission due to transmission of medium energy ions through free-standing single layer graphene.*, Uppsala/Sweden 24/06/2019 - 02/07/2019

Helmholtz-Zentrum Dresden-Rossendorf, Institute of Ion Beam Physics and Materials Research, RADIATE Proposal Nr. 19001755: *Light ion transmission through single and multilayer graphene*, Dresden/Germany 05/08/2019 - 09/08/2019

List of abbreviations

2D	two-dimensional		**IBA**	ion beam analysis
3D	three-dimensional		**ICD**	interatomic Coulombic decay
q_{in}	incident charge state		**MEIS**	medium energy ion scattering
q_{out}	exit charge state		**NC-AFM**	non-contact atomic force microscopy
a.u.	atomic units		**NIELS**	neutrals and ion energy loss spectrometer
AFM	atomic force microscopy		**RBS**	Rutherford backscattering spectrometry
amu	atomic mass unit(s)			
arb. u.	arbitrary unit(s)		**SHI**	swift heavy ion
BLG	bilayer graphene		**SLG**	single layer graphene
COB	classical over barrier (model)		**STEM**	scanning transmission electron microscopy
CVD	chemical vapour deposition			
e^{-}	electron(s)		**TDDFT**	time dependent density functional theory
EBIS	electron beam ion source		**TEM**	transmission electron microscopy
EBIT	electron beam ion trap			
ECRIS	electron cyclotron resonance ion source		**TLG**	trilayer graphene
			TMD	transition metal dichalcogenide
EDX	energy-dispersive x-ray spectroscopy		**TOF**	time of flight
ERD	elastic recoil detection		**vdW**	van der Waals
HCI	highly charged ion		Xe^{q+}	Xe ion with a charge state of $q+$
IAP	Institute of Applied Physics			

Contents

1 State of the art and objectives

Ion-solid interaction has been a main field of research over the past decades as it forms the basis for many important applications such as nano lithography [1] and ion implantation as is needed for doping of semiconductors [2]. Additionally, several analytical methods using ion beams rely on a good understanding of the interaction between the ions and a material. Rutherford backscattering spectrometry (RBS) [3], medium energy ion scattering (MEIS) and elastic recoil detection (ERD) [4] are just a few of those ion beam analysis (IBA) techniques [5].

In the beginning, research focused on the fundamentals of the ion's energy E dissipation in a material. The energy transfer on the ion's trajectory x in a material per unit path length is described by the stopping power

$$S = -\frac{\mathrm{d}E}{\mathrm{d}x} = S_n + S_e. \tag{1.1}$$

The stopping power S is made up of two constituents: nuclear stopping S_n and electronic stopping S_e. The first one derives from nuclear collisions whereas the latter describes the energy transfer due to excitation and ionisation of the target's and projectile's electronic system. Besides the case of low energy heavy particles as projectiles, the electronic energy transfer usually dominates [6].

Ions depositing sufficient energy in a material provoke radiation damage which can lead to structural modifications whereas nuclear stopping usually causes the most damage: nuclear collisions result in collisional cascades leading to sputtering which is one major application of ion-solid interaction. Another way of causing material modifications is provoking electronic excitations either via electronic stopping or neutralisation. Electronic excitations may then be converted into nuclear motion triggering material damage. For the latter, swift heavy ions (SHI) and highly charged ions (HCI) are special cases which are mainly interesting for fundamental research.

Examination of effects of the interaction of highly charged ions with materials advanced in the last quarter of the 20th century after development of ion sources that are able to produce ions of high charge states, e.g. electron beam ion traps/sources (EBIT/EBIS, cf. section 2.1) or electron cyclotron resonance ion sources (ECRIS) [7, 8].

In general describing the electronic interaction of ions with materials demands differentiating between effects induced by the kinetic or the potential energy, respectively and thus between

swift heavy and slow highly charged ions. This was done for instance by Aumayr et al. with regard to nano structuring [9]. As the main interest of this thesis is to gain further insights into the neutralisation processes of slow highly charged ions, this theoretical introduction will henceforth focus on HCIs.

1.1 Highly charged ions

Known phenomena occurring in ion-solid interaction such as nano structuring [10], sputtering [11–13] and electron emission [14] usually are associated with the kinetic energy of the impinging ion. Looking at highly charged ions, their potential energy also needs to be taken into account if studying the interaction with a material.

The potential energy of, for instance, a Xe ion with a charge state q, namely Xe^{q+} is made up of the sum of the binding energies of all q removed electrons from the atom. The potential energy of Xe^{q+}, which may easily excel its kinetic energy, is shown in dependence of the charge state q in figure 1.1 (a).

(a)   (b)
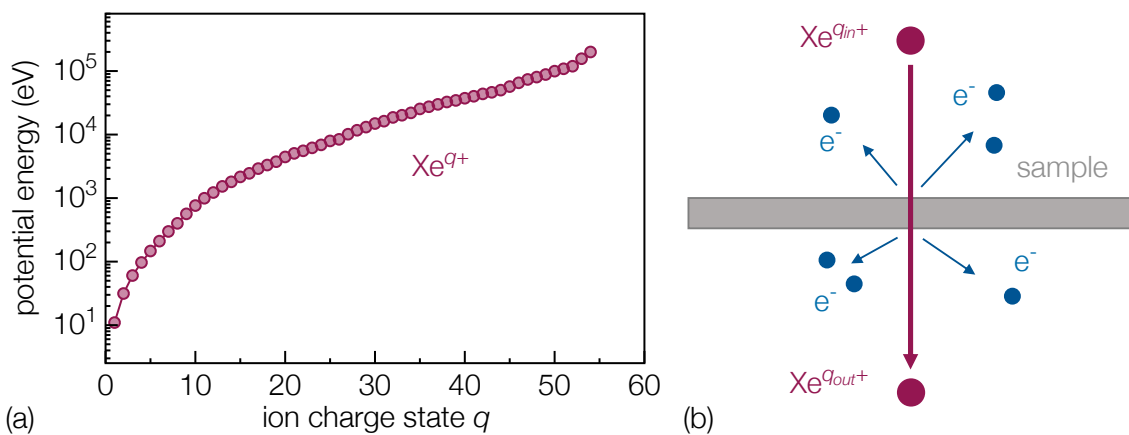
Figure 1.1: (a) Potential energy of Xe^{q+} ions in dependence of the ion charge state q. The potential energy results from the sum of the binding energies of all q removed electrons of the atom. (b) Electron emission due to the interaction with highly charged ions (only effects important for this thesis are included).

Deposition of this potential energy in a material may then also cause effects such as nano structuring, sputtering and electron emission mentioned before together with the kinetic energy of the projectile [15–18]. One notable difference nevertheless is the affected volume: in contrast to swift heavy ions (SHIs), HCI induced effects affect only the topmost atomic layers of a material. SHIs can be reckoned as the counterpart to HCIs because their interaction with materials is dominated by the high kinetic energy (and mass) of the projectile whose deposition affects also the bulk material and is mainly described by the energy loss or stopping power (cf. equa-

tion (1.1)) [19].

Of all mentioned effects, electron emission [20–22] is the most important one in our setup whereby in the relevant velocity regime kinetic electron emission only has a small contribution to the total electron yield and potential electron emission is the main underlying mechanism [23]. Using thin, here atomically thin materials such as a single layer of graphene (cf. section 1.2) as target we can still detect the projectile after interaction with our sample. Detecting both, emitted electrons due to interaction with the material and transmitted ions, makes coincidence measurements of electrons and ions possible (see experimental setup in section 2.2).

During transmission through the material, the impinging ion $Xe^{q_{in}+}$ also captures and stabilises several electrons from the sample and thus will be detected with a smaller charge state $Xe^{q_{out}+}$ with $q_{out} < q_{in}$. A scenario how this neutralisation may take place in combination with a short introduction into possible mechanisms is given in the following section. Figure 1.1 (b) illustrates the interaction of a highly charged ion with a thin target.

HCI neutralisation

Highly charged ions approaching a (metal) surface start interacting with the material even before they impact. In 1991 Burgdörfer *et al.* [24] described this process in the form of the classical over barrier (COB) model. According to COB, the ion captures electrons resonantly from the surface within a distance smaller than a critical distance R_C where the neutralisation sets in:

$$R_C = \frac{1}{2W}\sqrt{8q + 2} \tag{1.2}$$

In equation (1.2) which uses atomic units, q is the incident charge state of the impinging ion whereas W is the work function of the surface [24].

This model is applicable to slow HCIs as we use in our experiments since we reach projectile velocities of $v \lesssim 1$ a.u. $\sim 2.19 \cdot 10^6$ m/s.
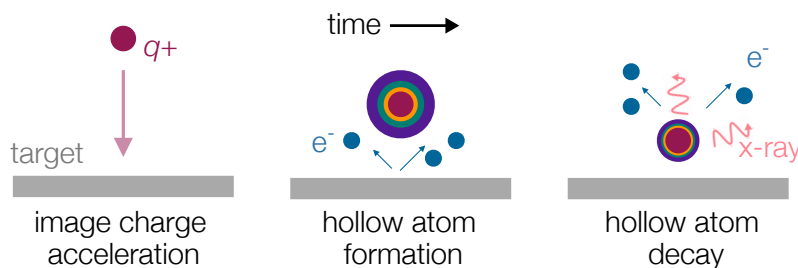

Figure 1.2: Hollow atom formation and decay of a HCI approaching a target surface.

These electrons are captured in high Rydberg states leading to a neutralised atom with empty inner states: a so-called hollow atom is formed [25, 26]. A sketch of the described steps in the

interaction of a highly charged ion with a material is given in figure 1.2 [27].

The hollow atom then further decays which means that intermediate energy levels are populated by electrons. Wilhelm *et al.* [28] described relevant mechanisms that possibly contribute to this decay which will be shortly presented below.
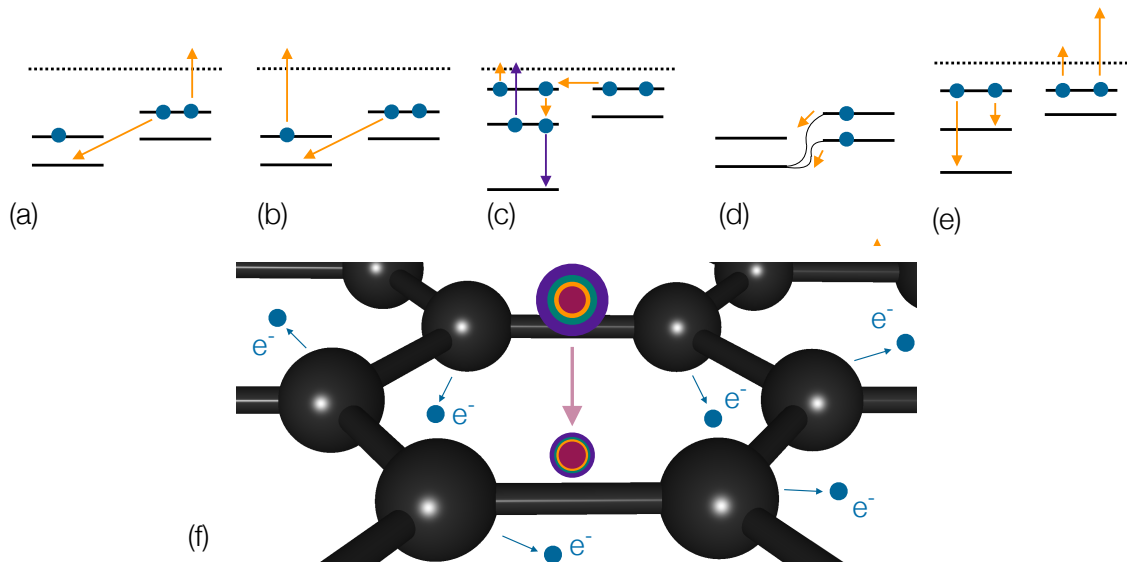

Figure 1.3: Deexcitation mechanisms: (a) Auger neutralisation, (b) exchange transition, (c) resonant transition and atomic Auger deexcitation, (d) sidefeeding, (e) resonant transition and interatomic Coulombic decay, (f) schematic presentation of the interatomic Coulombic decay in the interaction of a hollow atom transmitting a single layer of graphene.

Figure 1.3 displays four possible processes.

(a) Auger neutralisation: a target electron is transferred into a deeply bound projectile state, the excess energy is used to ionise another target electron

(b) exchange transition: a target electron is transferred into a deeply bound projectile state, the excess energy is used to ionise another electron of the projectile

(c) resonant transition and atomic Auger deexcitation: electrons are captured resonantly by the projectile (orange arrows) and decay (non-)radiatively further on (violet arrows)

(d) sidefeeding: a resonant transfer from deeply bound target to projectile states becomes possible due to energy level shifting at close distances

Moreover, Wilhelm *et al.* ruled out all of those processes because of considerations regarding time scales: measured neutralisation time constants of highly charged ions cannot be explained by such low rates that are associated with the mechanisms above [19, 28]. They introduced

a promising candidate which is consistent with experimental data: the interatomic Coulombic decay (ICD) which is depicted in figure 1.3 (e) and (f).

ICD (also called direct Auger deexcitation) describes a process where one projectile outer-shell electron fills an inner-shell vacancy. The excess energy is transferred to neighbouring atoms leading to emission of multiple electrons from different nearest (or next nearest) neighbours of the target into the continuum. ICD is dominated by a strong distance dependence $\left(\sim \frac{1}{R^6}\right)$ and was first described by Cederbaum *et al.* in 1997 [29] for HF molecules and later experimentally shown by Jahnke *et al.* [30, 31]. Due to the formed hollow atom with large orbitals, the necessary electron-electron interaction of projectile and target electrons can albeit be assumed which makes ICD applicable to HCIs.

With the interatomic Coulombic decay being a fast process it is also a possible solution to the time scale problem mentioned above and thus a good candidate for the description of the neutralisation process of a highly charged ion. ICD is not completely efficient so there will still be some unoccupied inner shell vacancies at the projectile after the interaction with the material. They can afterwards decay by short Auger electron emission cascades or otherwise decay radiatively under emission of x-rays [32]. The latter ones were also already observed experimentally for the system of highly charged Xenon ions transmitted through a single layer of graphene [33]. A theoretical model called TDPot uses time dependent potentials and also includes ICD rates for the description of the neutralisation dynamics of HCIs and was also published in 2019 [34]. It shows good agreement with experiments, which supports the idea of using ICD as main neutralisation process of HCIs.

1.2 2D materials

When K.S. Novoselov and A.K. Geim (Nobel prize in physics 2010 "for groundbreaking experiments regarding the two-dimensional material graphene" [35]) first reported the observation of a stable two-dimensional material, a monolayer of graphene, in 2004 [36] they laid the foundation for a new field of physics.

Having prepared their samples using mechanical exfoliation they were able to find single layers of graphene amongst mostly few layer graphene sheets. First experiments were performed to investigate the electronic properties of the new-found material concluding that "graphene may be the best possible metal for metallic transistor applications" [36]. However, it was not for long until other 2D materials were studied as well: in 2005 the Nobel laureates discussed electronic properties of other two-dimensional atomic crystals [37] investigated in field-effect-transistor-like devices such as single layers of boron nitride or transition metal dichalcogenides.

Two-dimensional materials have been a hot topic ever since offering promising optical and elec-

tronical properties [38]. Even more encouraging characteristics are expected from van der Waals (vdW) heterostructures which are obtained through combination (stacking (vertical) or sticking together (lateral) heterostructures) of 2D materials [39]. Addressed fields of possible applications using two-dimensional materials or vdW heterostructures range from tunnelling devices (field-effect tunnelling transistors) via photodetectors and phototransistors [38] to tunable light-emitting diodes [40–43] or molecular sieving possibilities [44, 45].

Various stable 2D materials were found until now and progress is still going on. Not all of them consist of one atomic layer only as it is the case for graphene. For instance, transition metal dichalcogenides (TMDs) such as MoS_2 or WS_2 are also called two-dimensional even though they consist of three atomic layers (cf. figure 1.5 below).

In general, 2D materials are defined by - if stacked onto each other to form a 3D material - a layered structure with strong covalent bonds in-plane and weak vdW bonds between layers. Definitions of two-dimensional materials differ as sometimes the ability of producing a free-standing layer of the material is referred to as another vital feature of a 2D material [46]. Sometimes all materials with a thickness of less than 10 atoms are counted as 2D materials [46].

In the following, a discussion of two of the most famous two-dimensional material families, graphene and transition metal dichalcogenides, is presented before a short summary on methods how to produce 2D materials. To conclude, recent studies on contaminations on 2D materials are reviewed.

Graphene

Graphene probably is the most well-known two-dimensional material [47] and can be considered as the basis of Carbon allotropes from dimension zero to three: fullerenes, carbon nanotubes, graphene and graphite. It can be seen as composed of benzene rings without the hydrogen atoms: graphene forms a honeycomb structure which is shown in figure 1.4 (a)-(c).

The thickness of a 2D material is usually assumed to be the interlayer spacing of its 3D counterpart, here addressing graphite with an interlayer spacing of d = 3.4 Å [48]. The C-C bond length amounts to 1.42 Å [49].

Graphene possesses multiple extraordinary electronic properties which are presented in detail in [50]. It is a zero band gap semiconductor (also called semimetal), as the valence and conduction band touch only at the K point.

Rebuilding bulk graphite via stacking several layers of graphene onto each other (A-B-A stacking) produces bi- and trilayer graphene. The latter one can be seen in figure 1.4 (d)-(f).

Today, single to trilayer graphene is commercially available, e.g. at Graphenea [51]. More information on how free-standing graphene is used as target material in our experimental setup can be found in section 2.2.
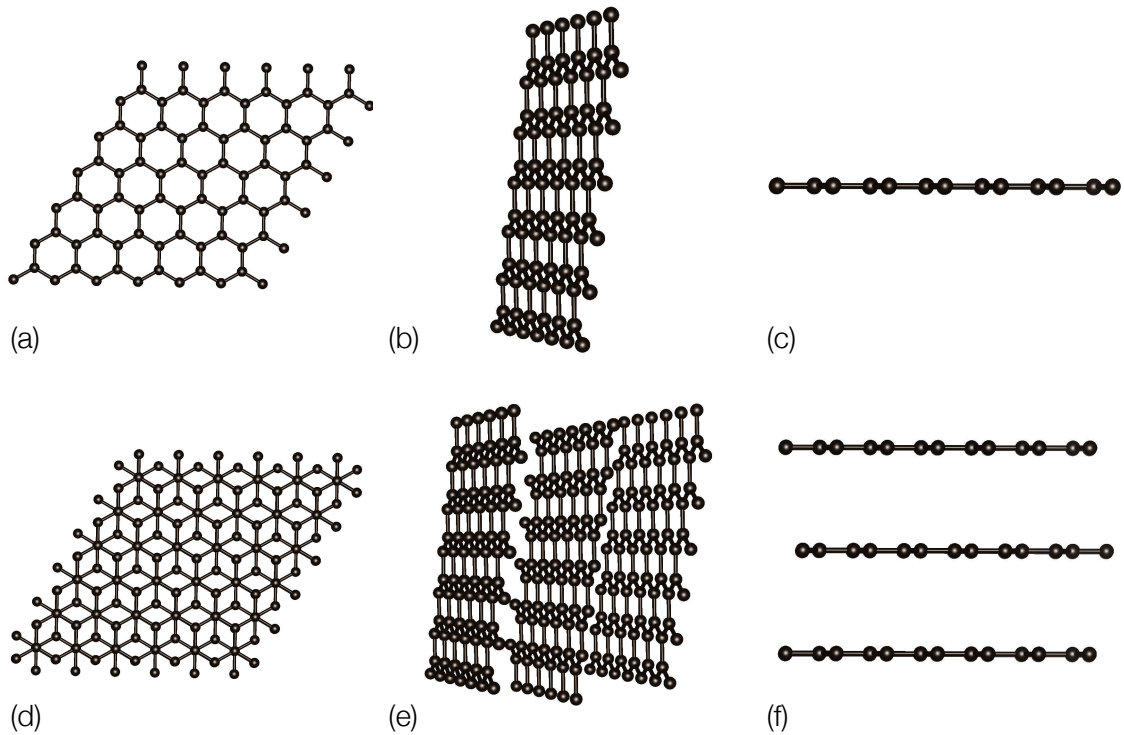
(a)   (b)   (c)

(d)   (e)   (f)

Figure 1.4: Various perspectives of the structure of single layer (a-c) and trilayer (d-f) graphene.

Transition metal dichalcogenides

Besides graphene, transition metal dichalcogenides make up another group of 2D materials with the universal formula MX_2. Nominally, M is a transition metal whereas X is a chalcogen (elements of group 16 in the periodic table of elements).
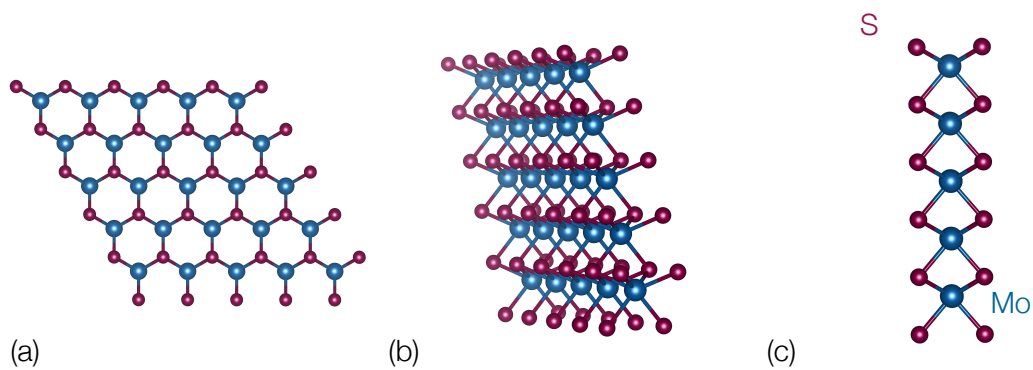

S

(a)   (b)   (c)   Mo

Figure 1.5: Various perspectives of the structure of TMDs (e.g.: MoS_2).

Depending on the transition metal, TMDs can either be insulating, semiconducting, metallic or semimetallic [38]. All of them consist of three atomic layers: the transition metal is sandwiched between two layers of the chalcogenide - still building a hexagonal structure. Representatively,

molybdenumdisulfide (MoS_2) is portrayed in figure 1.5.

Even though the hexagonal structure (figure 1.5 (a)) of TMDs and the one of single layer graphene (figure 1.4 (a)) look alike, lattice dimensions are larger in this case with a Mo-S bond distance of 2.42 Å leading to a lattice constant of 3.18 Å [52]. In contrary to bulk MoS_2 (indirect), single layer MoS_2 is a direct semi-conductor [53].

Preparation of 2D materials

With graphene and other 2D materials being handled as promising candidates for future devices a lot of effort was put into the development of production and processing mechanisms for two-dimensional crystals. Figure 1.6 depicts two prominent production [54] and two transfer processes [55] for 2D crystals. Described methods (upon many others) are discussed in [56] and summarised below.
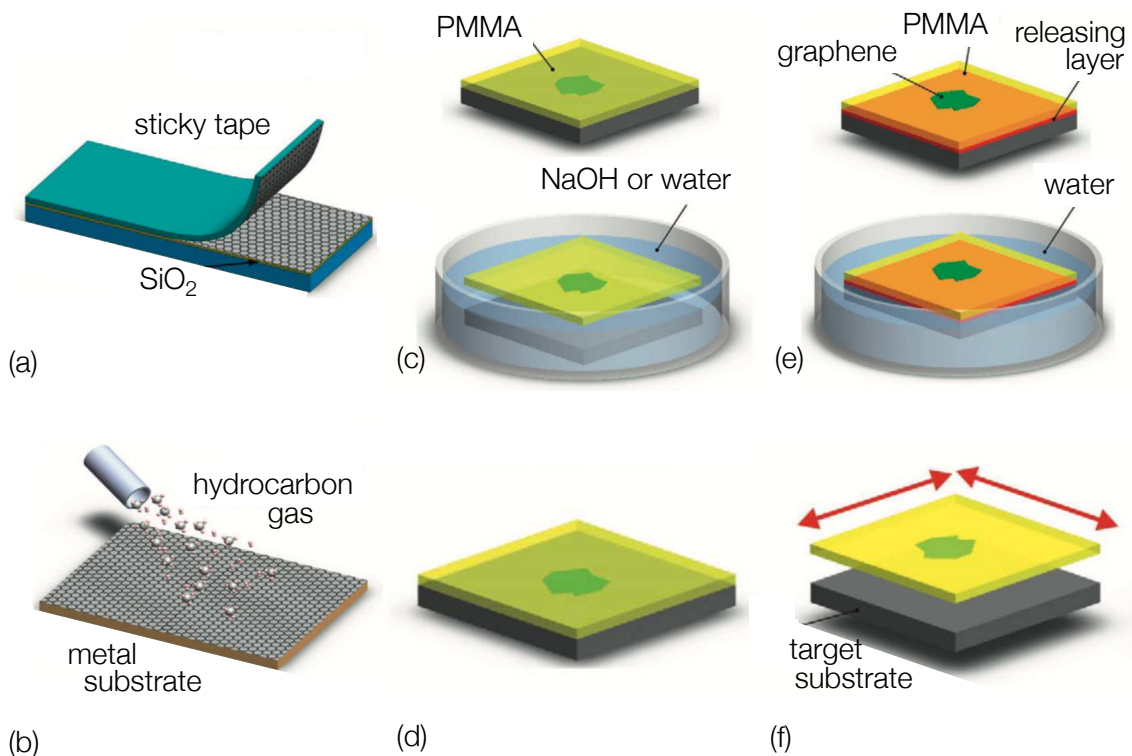

Figure 1.6: Production and transfer mechanisms of two-dimensional materials: (a) micromechanical exfoliation, (b) chemical vapour deposition, (c)-(d) wet transfer method, (e)-(f) dry transfer method. Schematics taken from [56].

(a) micromechanical exfoliation: Layers of the bulk material are split via mechanical forces, e.g. rubbing of a graphite surface on another flat surface.

(b) chemical vapour deposition (CVD): A vaporized precurser (hydrocarbons) is deposited onto a substrate (e.g. thermally driven or plasma enhanced).

(c) wet transfer method (part 1): A poly(methyl methacrylate) (PMMA) layer is deposited on the sample, e.g. graphene on substrate and then immersed in NaOH solution. The polymer is released upon etching of the substrate.

(d) wet transfer method (part 2): The sample with its PMMA layer is then transferred onto the target support. Acetone finally dissolves the PMMA and releases the sample.

(e) dry transfer method (part 1): The sample is deposited onto one water dissolvable and one PMMA layer. Dissolving the lower layer leads to the PMMA and sample layer floating on water, however without contact between sample and water.

(f) dry transfer method (part 2): The floating film is then transferred onto the target support.

Both transfer techniques do not leave the sample completely uncontaminated as for instance residuals of the sacrificial PMMA layer may still get trapped on the sample besides other adsorbates.

Contaminations on 2D materials

Since the special aspect of two-dimensional materials is their atomically thin thickness, everything challenging this fact is a major issue. Every form of contamination on either side of the material may change its properties. This fact was already addressed in the very first paper on graphene in 2004 [36]. Novoselov *et al.* reported on changes in their measurements when annealing few layer graphene which they attributed to unintentional doping by water.

In fact, graphene is known to be densely covered with contaminations - mostly hydrocarbons in various stoichiometry (C=O, C-OH, H-C) and chain length, water and possibly residuals from transfer processes (e.g. PMMA) [39, 57–59]. In case of CVD growth on metallic surfaces also metal contamination from the production (e.g. Cu, Ni, Fe) can be found [60]. Figure 1.7 shows STEM images of single layer graphene (monolayer nature was verified via atomic-resolution STEM (middle)) where the thickness of hydrocarbon adsorbates is given in equivalent number of graphene layers [61].

When stacking 2D materials the relation of the affinity between two layers and the affinity between the 2D crystal and the contaminant needs to be considered. So, e.g. if graphene is deposited on substrates it has only poor adhesion to (as for example mica), contaminations are found uniformly across the whole surface. In contrary, if the energetically favourable situation is the largest possible common interface, contaminations are forced away leading to formation of bubbles. This effect was found for graphene on MoS_2, hBN and WS_2 as well as for heterostructures. These bubbles are sometimes also called dirt pockets [38, 62].

Moreover, contaminants can have a crucial influence on the behaviour of a 2D material. Zan *et al.* [63] found that under electron irradiation (as used in TEM) contaminations are used for hole
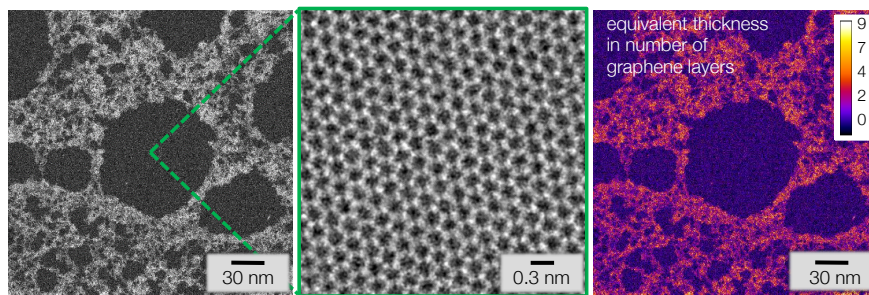
Figure 1.7: (left) STEM image of SLG showing clean monolayer regions, (middle) atomic-resolution STEM image of a clean region as seen in the left picture confirming the thickness of only one atomic layer, (right) colour-coded version of the left picture with estimated thicknesses of hydrocarbon contaminations obtained via high angular annular dark field (HAADF) STEM. Taken from [61].

healing provoking a self-healing mechanism. TEM images showing this hole filling process at the border of hydrocarbon contaminations are depicted in figure 1.8. For MoS_2 as well as for graphene it was found that contaminations have a detectable effect on its work function [53]. Thus, finding a method to decontaminate 2D materials has been an important topic recently.
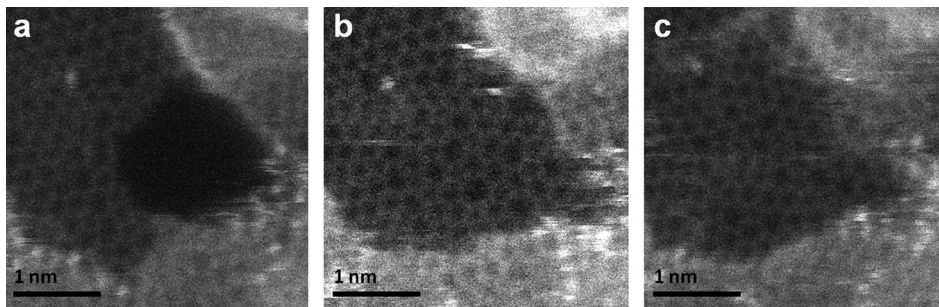

Figure 1.8: Self-healing mechanism of free-standing single layer graphene. Holes in graphene at the border of hydrocarbon contaminations are closed under electron beam irradiation in TEM. Taken from [63].

The most common way to deal with contaminations is annealing the sample. Investigations with Raman spectroscopy about the thermal stability of graphene in air [64] and vacuum [65] showed no defects in graphene layers until 500°C and 900°C, respectively. In case of annealing in air, reactions of graphene with O_2 affect C-O bonds which leads to instability. Kim *et al.* [66] even reported on the stability of free-standing graphene up to at least 2300°C. Hence, if annealing up to hundreds of degrees Celsius removes adsorbates, this can be done without affecting the graphene sample.

Many examples can be found in literature how annealing is employed to clean two-dimensional materials. Mainly, graphene samples are heated up either in Ar/H_2 environment [54, 55] or in vacuum [58, 60, 67, 68]. Although, used temperatures and durations vary between 280°C (ultra

high vacuum) [56, 68], 360-400°C (2-4 hours, Ar/H$_2$) [54, 55] and 500°C (10 minutes, vacuum $\sim 10^{-9}$ mbar) [58] up to 750°C (3 minutes, vacuum) [67]. Also metallic contamination remaining from CVD on metal surfaces can be reduced via annealing the sample at 500°C (30 minutes, vacuum) [60]. Cleanliness - the ratio of clean vs. contaminated area of a sample - of graphene in general is determined via TEM [57, 67, 69], AFM [68] or Raman spectroscopy [57, 65, 68, 69], sometimes also via x-ray photoelectron spectroscopy [56, 57, 68].

However, van Dorp *et al.* [58] also stated that contamination can get fixated under electron irradiation (as in TEM) and thus is still present after heating the sample. This is explained via crosslinking of hydrocarbons and graphene under influence of electron irradiation and needs to be considered when analysing annealing success via TEM.

One study [57] even went one step further and described the decomposition of PMMA in a two-step scheme: air-facing PMMA layers are decomposed at lower temperatures (starting at 160°C but still not entirely removed even after annealing at 350°C for 5 hours) than the graphene-facing PMMA layer which begins to burn out at 200°C. Annealing at more than 250°C did not yield higher cleanliness. Leftovers of PMMA forms strip-like patterns (also wrapping nanoparticles).

Algara-Siller *et al.* [59] reported better cleaning in case of dry-cleaning: they annealed their samples at moderate temperatures embedded in adsorbents, e.g. activated Carbon.

While most studies focused on cleaning of graphene, one can also find studies on MoS$_2$: Oche-dowski *et al.* [53] heated MoS$_2$ to 200°C for 30 minutes in vacuo before performing non-contact atomic force microscopy (NC-AFM) measurements to clean the sample from contamination adsorbed in ambient. Annealing reportedly also removes contaminants remaining from stacking (wet transfer technique) vdW heterostructures [38].

Additionally, annealing does not only serve the purpose of cleaning samples but can also be used for applications: Ni *et al.* [65] found that vacuum annealing makes graphene more active to molecular adsorption (H$_2$O and O$_2$ in particular). Heating samples again helps to desorb particles (until exposed to air again). This effect can also be used for doping which may be attractive for electrical devices.

There are various possibilities to achieve heat treatment in air (hot plate) and vacuum, e.g. radiative heating or resistively heating via a heating wire. Laser annealing is another way to heat samples, albeit estimating the treatment temperature is more difficult in this case [67].

Besides annealing, other cleaning techniques were demonstrated. For instance, as annealing is not really feasible at low temperatures in a cryostat other ways for sample cleaning had to be developed. Moser *et al.* [70] cleaned their samples via inducing high current densities ($I \sim$ mA) through graphene devices. Graphene can withstand such extreme conditions while the adsorbed contaminations on the surface are removed via effects induced by the large electrical current such als Joule heating. Other mentioned cleaning techniques are for instance chemical cleaning (chloroform) or mechanical cleaning (scanning the surface with an AFM tip) [56].

1.3 Motivation

Highly charged ions have proved themselves as an effective tool to study and modify 2D materials: e.g. insight into defect engineering by ion irradiation will be valuable information since the formation of pores of specific sizes will be handy for possible applications [71, 72].

The other way around, 2D materials are also an effective tool to study the neutralisation of highly charged ions because the ion has not yet reached its equilibrium charge state after transmission. Gruber *et al.* [61] investigated the interaction of highly charged Xe with a single layer of graphene showing ultrafast neutralisation of the projectiles. They measured the mean number of captured and stabilised electrons for impinging ions with various velocities. The dependence of the mean number of captured electrons from the interaction time with the target was fitted by

$$q_{in} - \overline{q}_{out} = q_{in} \left(1 - e^{-\tau/\tau_n^{exp}} \right).$$

(1.3)

There, τ_n^{exp} is a fit parameter giving a neutralisation time constant and τ is the interaction time given as the ratio of an effective interaction length d_{eff} and the velocity v of the projectile:

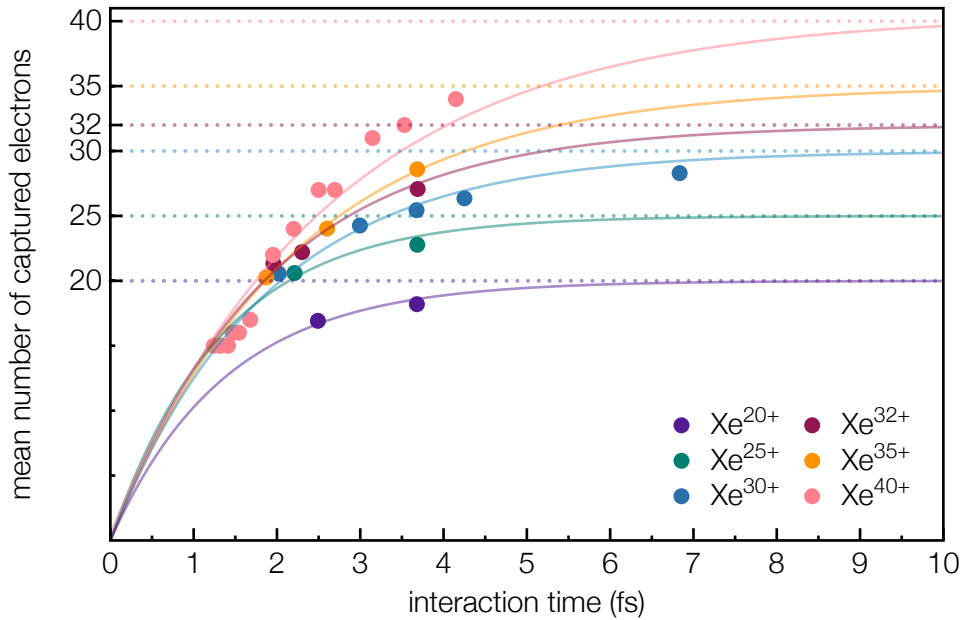$$\tau = \frac{d_{eff}}{v}.$$

(1.4)

Figure 1.9: Mean number of captured and stabilised electrons after transmission of $Xe^{q_{in}+}$ through a single layer of graphene. Data points for Xe^{20+} to Xe^{35+} are taken from [61], points for Xe^{40+} is unpublished data measured by Janine Schwestka.

According to performed time dependent density functional theory (TDDFT) calculations [19] and the COB model (equation (1.2)), the effective neutralisation length (distance in which the interaction takes place) is assumed as

$$d_{eff} = (0.573\sqrt{8q+2} + 1.66) \text{ Å}. \tag{1.5}$$

Experimental data processed as described above is shown in figure 1.9. Data for Xe^{20+} to Xe^{35+} is taken from [61]. Charge dependent neutralisation times in the order of $\sim$ fs can be extracted from plotted fits according to equation (1.3), which are a significant component in time scale considerations to possibly participating neutralisation mechanisms as discussed in section 1.1.

However, equation (1.5) builds upon a clean graphene target. Contaminations on the sample may thicken it by various monolayers. Therefore, using cleaned samples could result in higher neutralisation time constants as well as in the possibility of other participating deexcitation mechanisms which would not be necessary to consider otherwise. Thus, knowledge on the cleanliness of our sample is crucial to pursue estimations on neutralisation times which is the motivation for the present study. Cleaning processes in the form of heat treatment of our samples shall be applied to review the influence on contaminations in the interaction and neutralisation of highly charged ions.

2 Experimental methods

Measurements discussed in this diploma thesis were performed at the Neutrals and Ion Energy Loss Spectrometer (NIELS) facility of the Atomic and Plasma Physics Group at TU Wien. The experimental setup is presented in the current chapter following a brief description of the employed electron beam ion source.

2.1 Electron beam ion source

Ionisation by electron collision is the main mechanism used to produce ions in an electron beam ion source (EBIS). To achieve highly charged ions, it needs to be ensured that working gas atoms stay in the collision area long enough so that multiple electrons can get removed in subsequent electron impact events. Therefore, ions are held in a potential trap within three drift tubes (U_0, U_a, U_b) and brought to collision with a high density electron beam (obtained via magnetic compression) to subsequently ionise electrons. A schematic of an EBIS is shown in figure 2.1.
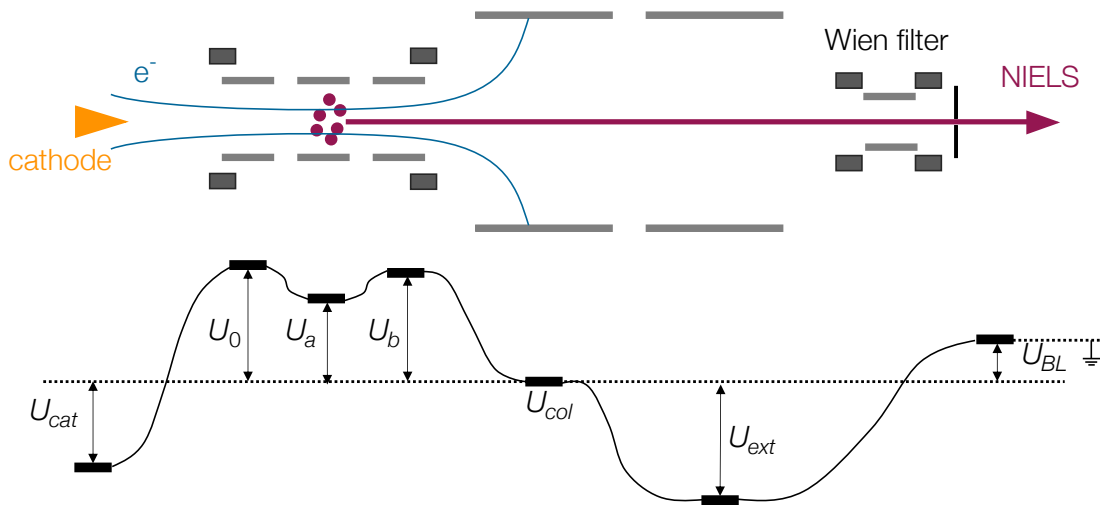

Figure 2.1: Schematic overview of an EBIS. Working gas ions are held within a potential trap and get ionised by a high density electron beam. Ions are extracted and specific charge states are selected by means of a Wien filter.

The behaviour of U_b defines whether the ion source is operated in leaky mode ($U_b = $ const. $< U_0$) or in pulsed mode, when U_b switches from U_{b_1} to $U_{b_2} < U_{b_1}$ for a short time

in the order of ms. Hence, U_b (U_{b_2} in pulsed mode) defines the kinetic energy of the extracted ions. Biasing the source to U_{BL} (BL = beamline) decelerates the ions towards entering the target chamber resulting in a final kinetic energy E_{kin} of

$$E_{kin} = q \cdot (U_b - U_{BL}).$$ (2.1)

A Wien filter is located before the entrance to the target chamber. Depending on applied voltages, selected charge states of the employed working gas (in case of Xenon, charge states in the range of Xe^{1+} to Xe^{44+}) can enter the target chamber covering kinetic energies from 1 - 350 keV (equation 2.1). Multiple electrostatic lenses at various positions are employed to focus and steer the ion beam onto the target as desired [73, 74]. A Dreebit Dresden EBIS-A [75] with xenon or argon as working gas at an operating pressure of roughly 4-5·10⁻⁹ mbar was used for the measurements presented in this thesis.

2.2 Ion beam spectrometer

The ions extracted from the ion source then enter the target chamber, schematically sketched in figure 2.2. The spectrometer is described in detail in [76].
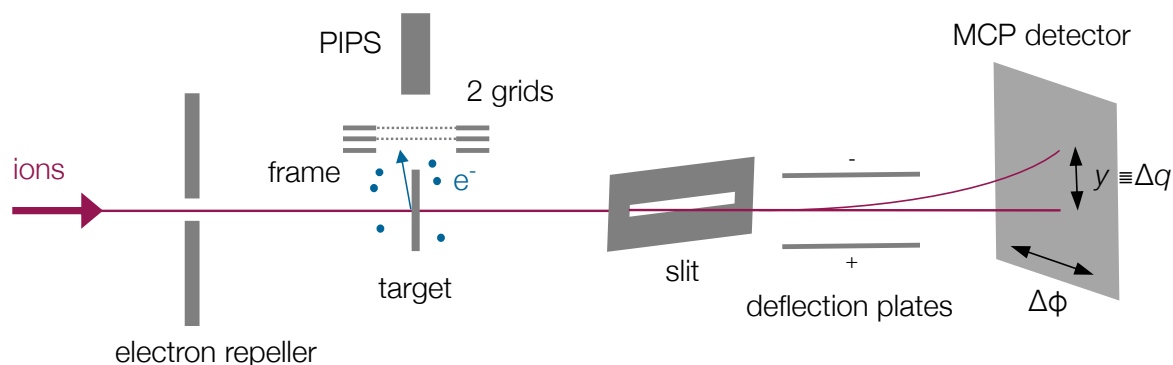

Figure 2.2: Schematic overview of the target chamber at the NIELS setup. The electron repeller as well as the two grids, the frame and the PIPS detector are further collectively referred to as electron emission statistics and are discussed later on in this chapter. A slit and deflection plates in combination with a MCP detector are employed for exit charge state analysis of ions transmitted through 2D samples.

First, the ion beam passes through a set of one vertical and one horizontal shaping slit with two possible slit widths each (0.5 mm and 1.0 mm, both not depicted in figure 2.2). A target holder is mounted in the centre of the chamber and can be translated in three directions and rotated around the vertical axis. The electron repeller, the frame, the two grids and the passivated implanted planar silicon detector are in use to collect and count electrons emitted from the

sample and are further described later on in this chapter. A pre-vacuum and a turbo pump ensure a pressure of $< 5.0 \cdot 10^{-9}$ mbar in the target chamber.

Another horizontal slit, deflection plates and a microchannel plate (MCP) detector are used to analyse the mean exit charge state of the ions transmitted through probed samples. The principle of this spectroscopy is further described below.

All examined 2D materials are placed on transmission electron microscopy (TEM) grids with a Quantifoil (QF) support on top. On some samples, an additional Au layer of 50-100 nm covering the QF sits in-between the QF and the actual sample of interest. The TEM grids have a diameter of 3 mm. Most of the more recent samples used for this project were produced by Graphenea on a 300 mesh Au TEM grid with a Au coated QF ($\sim$ 50 nm) having a hole size of 2 μm and a space between two holes of 4 μm [51]. The structure of the samples is outlined in figure 2.3 (a) whereas microscopy images of a single layer graphene (SLG) sample are depicted in figure 2.3 (b) (light-optical microscope, magnification $\sim$ 200x) and figure 2.3 (c) (atomic resolution STEM, scale bar denoted inside the figure, [61]).

The Au coated QF serves the purpose of stopping ions from transmitting the support. Au layers with a thickness of 50-100 nm on the QF suffice to stop or adequately decelerate transmitted ions to be able to separate them from the ions of interest transmitted through the free-standing two-dimensional material.
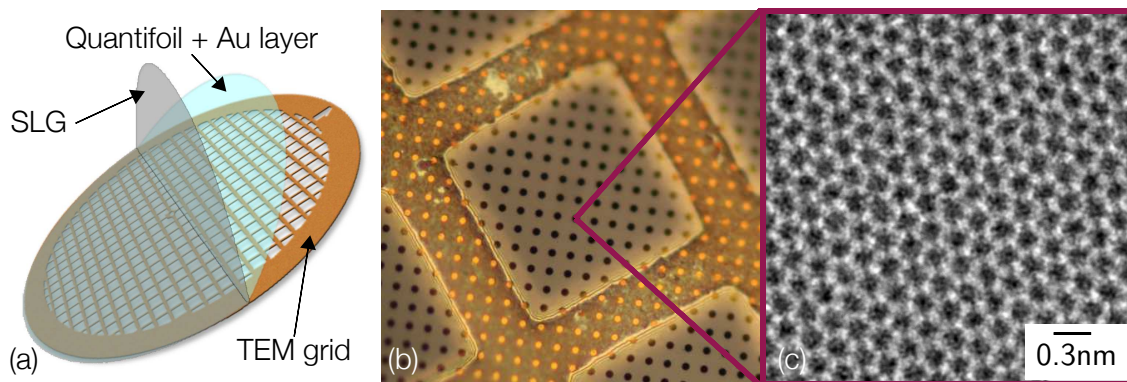

Figure 2.3: (a) Schematic of the used samples: the 2D materials (here single layer graphene (SLG)) are placed on a Quantifoil support (10-20 nm) coated with Au (50-100 nm), both on top of a standardised Au TEM grid. Picture taken and adapted from [77]. (b) Microscopy image (magnification $\sim$ 200x) of a SLG sample showing the Au TEM grid as well as the QF support (in this case with a 50 nm Au layer). (c) Atomic resolution STEM image of single layer graphene. Taken from [61].

Our target holder can hold three samples of this kind at the same time which are separately pinched between the main plate of the target holder and one smaller part for each sample (cf. figure 2.4). The conical openings allow to detect electrons emitted within an emission angle of $\alpha \leq 60°$.

To heat the sample holder to more than 300°C, a heating wire was mounted on the target holder. A 1Ncl15 wire with a room temperature (RT) resistance of $R = 1.0\,\Omega$ served for this purpose needing $\sim 5\,A$ to heat up the target holder and samples to 360°C. Two drilling holes through the metal plate serve as path for the horizontal parts of the wire. This ensures optimal contact area to pass on the heat to the target holder. To keep track of the sample temperature a PT100 or PT1000 temperature element was also mounted on the target holder.

Additionally, also for heating purposes, a Lasertack 6 W 445 nm laser diode [78] aligned to the sample was installed at NIELS.
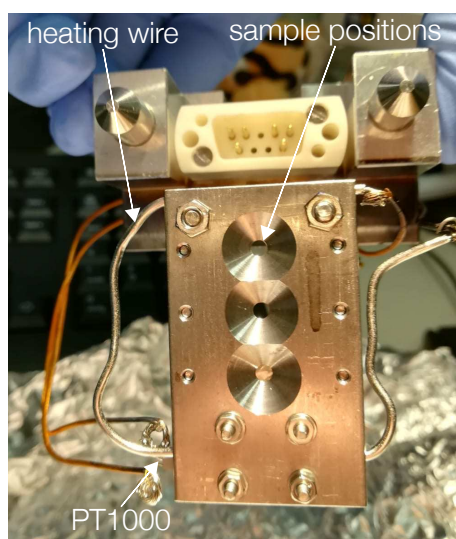

Figure 2.4: Photograph of our target holder. Three TEM grids supporting suspended 2D materials can be mounted in the target chamber at the same time. A 1Ncl15 heating wire ($R_{RT} = 1\,\Omega$) can be used to heat up the samples to > 300°C. To keep track of the temperature of the target holder, a PT1000 temperature element was installed.

Electron emission statistics

Emitted electrons from the sample are detected and counted by means of an electron emission statistics setup. Two highly transparent grids are used to attract the emitted electrons. By biasing the second grid less positively than the first one, the minimal energy of electrons transmitted through the second grid can be adjusted. Via variation of this potential difference, these retarding grids help to determine the energy of emitted electrons [23]. Presented measurements using the laser, however, were recorded after having unmounted one of the grids from the target chamber.

A negatively biased frame in front of the first grid is needed to attract the electrons to the transparent grid area instead of the positively biased frame of the first grid. A negatively biased electron repeller opposite of the sample holder also helps to guide the electrons to the grids (see figure 2.2).

Behind the two grids, the electrons are accelerated onto a passivated implanted planar silicon

(PIPS) detector biased at 25-30 kV. Impinging electrons on the detector create electron-hole pairs. The electric field of an applied bias voltage gathers these electron-hole pairs at the electrodes where they are then analysed by further acquisition electronics. All electrons arriving within the integration time of a used preamplifier are collected in one pulse with the pulse height being proportional to the deposited energy E_{dep}:

$$E_{dep} = N_e \cdot 30 \, \text{keV}, \tag{2.2}$$

where N_e is the number of collected particles, i.e. the number of detected electrons. This makes it possible to gather the mean value of emitted electrons due to a single ion impact by analysing the spectrum showing the pulses of the detector. These pulses are also used as start signal for time of flight measurements. Table 2.1 reports values for these parts of the electron emission statistics setup used for 150 keV Xe^{30+}. Figure 2.5 shows three electron emission statistics spectra of 87 keV Xe^{q+} transmitted through a free-standing single layer of graphene.

Table 2.1: Applied voltages on the electron emission statistics setup for 150 keV Xe^{30+}.

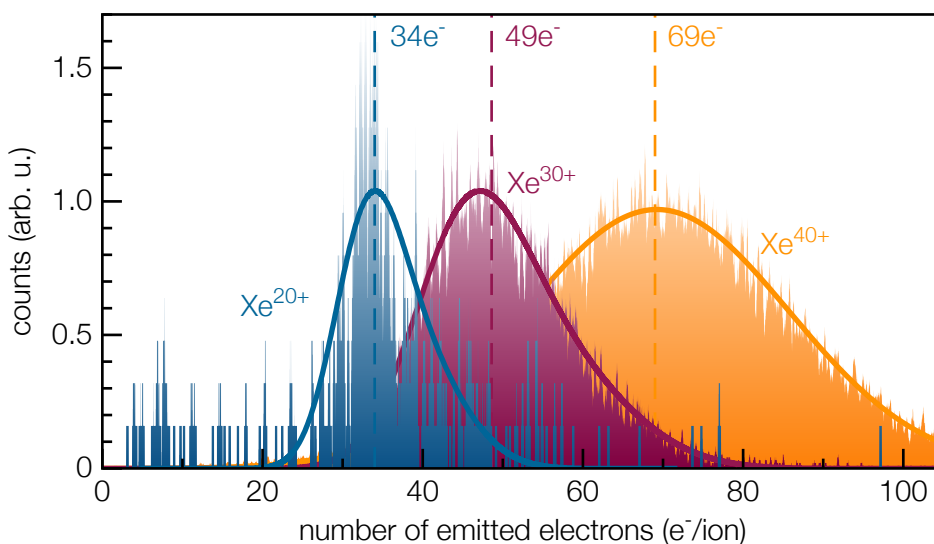| grid 1	270 V
grid 2	280 V
frame	-50 V
electron repeller	-300 V
PIPS detector	27 kV

Figure 2.5: Exemplary electron emission spectrum emitted due to interaction of 87 keV Xe^{q+} ions with suspended single layer graphene. The number of emitted electrons increases with the potential energy of the impinging projectile.

19

Repetition of measurements and comparison with published results from well-studied samples [79] can be consulted to estimate the electron collection efficiency. As another way to achieve knowledge about the collection efficiency, we performed simulations with the C++ library IBSIMU [80].

IBSIMU uses Vlasov iteration to solve the Poisson equation in a defined geometry. CAD files can be imported to do so as accurately as run-time permits it. A simplified version of our target chamber had to be modelled which is shown as a screenshot of the IBSIMU visualisation in figure 2.6 (a).

Particles can be added to the geometry to simulate particle trajectories which can then be further analysed, e.g. counting the electrons transmitted through the grids to estimate the electron collection efficiency. Figure 2.6 (b) shows the simulated trajectories for 40 keV Xe^{40+} ions (yellow, beam diameter 2 mm) and electrons emitted with a starting energy of 2.5 eV (red) within a horizontal cut through the target chamber (blue). Potential lines are shown in green colour. The electrodes were biased to $U_{repeller} = -250$ V, $U_{grid_1} = 490$ V, $U_{grid_2} = 500$ V, $U_{frame} = -50$ V and $U_{curtains} = 0$ V. Grounded curtains were additionally mounted in the target chamber for measurements tailored to analyse electron emission yields.
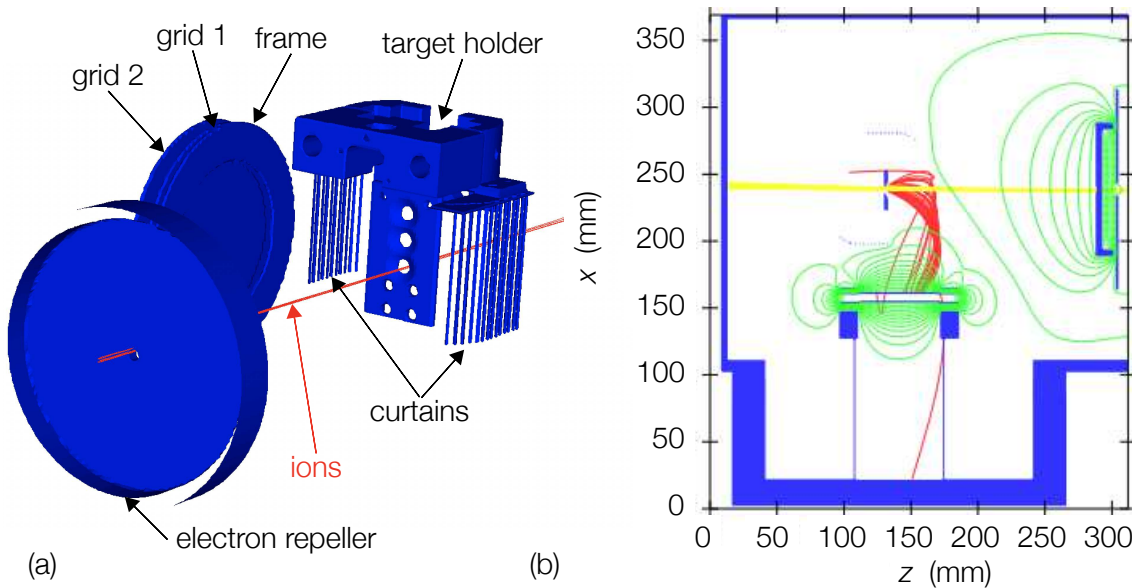

Figure 2.6: (a) Screenshot of the visualised geometry (imported via CAD files) in IBSIMU [80].
(b) Simulated ion (yellow) and electron with a starting energy of 2.5 eV (red) trajectories for 40 keV Xe^{40+} as projectile shown in a horizontal cut through the target chamber. Applied voltages are stated in the text.

Unfortunately, quantitative results cannot be made employing these simulations as the obtained collection efficiency depends crucially on various unknown parameters such as the energy and the emergence angle of emitted electrons, respectively. It is yet possible to observe a trend

of decreasing collection efficiency with the emission point of the electrons moving further away from the centre of the sample and hence closer to the edge of the target holder.

This is especially important if measurements with various (low) kinetic energies are executed without tuning the setup for each energy (to maintain the same parameters for all measurements). In this case, deflection of the incident ion beam due to applied voltages on the grids and frame leads to small shifts in the position of the sample interacting with the HCI and emitted electrons. Thus, stronger deflection in case of lower energies may also result in a lower electron collection efficiency.
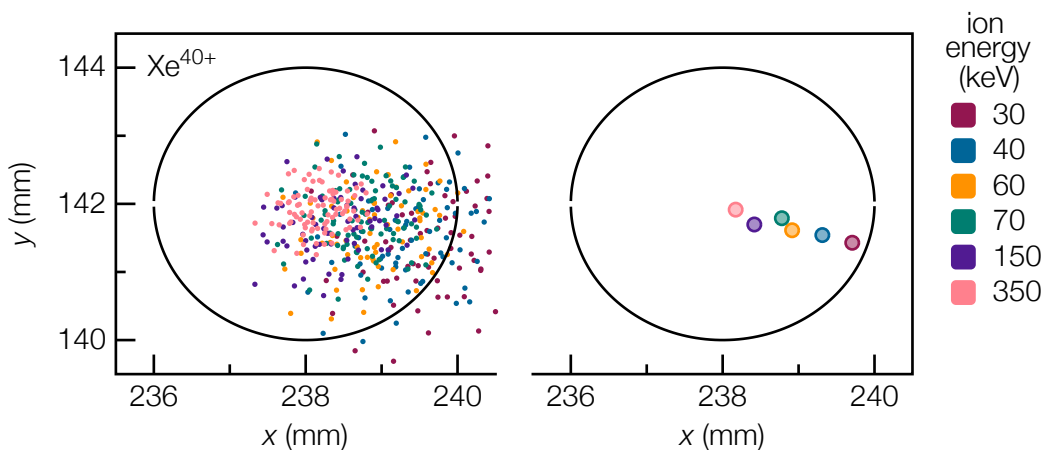

Figure 2.7: Ion impact position for Xe^{40+} with various energies. The black circle portrays the hole in our target holder hosting the 2D samples. The left part of the figure shows 100 simulated impacts 2 mm before the target whereas the right part represents the mean impact position for each energy.

This effect can be seen in figure 2.7. The left part of the graph shows the impact positions of 100 ions each for six energies (colour coded as denoted in the right part of the figure) whereas the right part shows only the mean impact positions. A tendency of the ions to be deflected downwards as well as to the right is observable.

Charge state analysis

When ions interact with a material, they scatter at target atoms leading to a change in momentum and often a change in direction. Additionally, HCIs capture (and stabilise) various electrons while interacting with the sample.

In case of very thin samples (e.g. two-dimensional materials) and ions with sufficiently high energies, ions can still be detected after transmission through the sample. Our setup to analyse both, the scattering angle as well as the exit charge state of the projectiles is presented below. The used target holder (cf. figure 2.4) has cones with an opening angle of 60° not suppressing scattered particles. To be able to analyse the exit charge state of the projectile after in-

teraction with the sample, we use a horizontal slit to cut out one plane of scattered particles. Those are then entering a pair of deflection plates (length $a = 39.6\,\mathrm{mm}$, distance of the plates $d = 21.15\,\mathrm{mm}$), where ions with different charge states q_{out_1} get stronger deflected than ions with charge states q_{out_2} for $q_{out_1} > q_{out_2}$.

Ions then continue on to a microchannel plate detector (MCP) with a delay line anode provided by RoentDek (DLD40, active area $> 40\,\mathrm{mm}$) in a distance of $b = 210\,\mathrm{mm}$. serving as a position sensitive detector. The measured deflection in relation to a neutral beam going through the deflection plates Δy in dependence of the ion charge state can be calculated according to equation (2.3) which is also sketched in figure 2.8.

$$\Delta y = \frac{1}{2}\frac{U \cdot q_{out}}{E_{kin}}\frac{a}{d} \cdot \left(\frac{a}{2} + b\right) \tag{2.3}$$
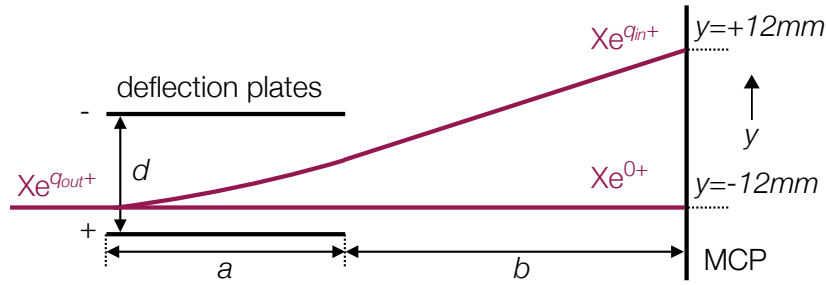

Figure 2.8: Schematic drawing of the charge state analysis setup at NIELS: Ions having a charge state of q_{out} after interaction with a sample enter a pair of deflection plates and get stronger deflected corresponding to their charge states. The charge state spectrum measured at a position sensitive MCP then ranges from neutral particles to particles with a primary charge state of $Xe^{q_{in}+}$.

The MCP position together with the deflection pair voltage is usually adjusted so that a neutral beam impinges at $y = -12\,\mathrm{mm}$ whereas the primary beam with an incident charge state of q_{in} hits the detector at $y = +12\,\mathrm{mm}$, leading to a maximum deflection of $y = 24\,\mathrm{mm}$. Thus, the conversion from y to charge state can be performed with equation (2.4).

$$q_{out} = (y + 12\,\mathrm{mm}) \cdot \frac{q_{in}}{24\,\mathrm{mm}} \tag{2.4}$$

The x-coordinate in recorded MCP spectra corresponds to the scattering angle of the detected ions. Additionally, the time of flight chamber is rotatable as a whole within $\Delta\varphi = \pm 8°$ making it possible to record scattering patterns in this angle area. The conversion of x position on the MCP with a chamber rotated to φ (as labelled on the spectrometer, given in degree °) to scattering angle φ can be done as follows in equation (2.5).

$$\varphi = \left(\mathrm{atan}\left(\frac{x}{1106\,\mathrm{mm}}\right) \pm 0.0181\varphi \right) \frac{180°}{\pi} \tag{2.5}$$

The factor 0.0181 arises from the scaling factor referring to the scale mounted at the back of the spectrometer. The distance between the target and the MCP measures 1106 mm, whereas the distance from the target to the scale is 1381 mm. 1° on the scale corresponds to $\sim 25\,\mathrm{mm}$.

$$\mathrm{atan}\left(\frac{1°\ \mathrm{on\ scale}}{\mathrm{distance\ target-scale}}\right) = \mathrm{atan}\left(\frac{25\,\mathrm{mm}}{1381\,\mathrm{mm}}\right) = 0.0181$$

The data acquisition is performed with RoentDek's COBOLD PC software [81]. A demo spectrum showing the exit charge state spectrum of 146 keV Xe^{30+} transmitted through a single layer graphene is given in figure 2.9. The conversion from x and y (lower and left axis) to scattering angle and exit charge state is noted at the upper and right axis, respectively. The right part of the graph shows the projection of counts on the y axis (or exit charge state axis) which will also often be used for analysis (rotated 90° as to counts vs. exit charge state) in the following chapter.
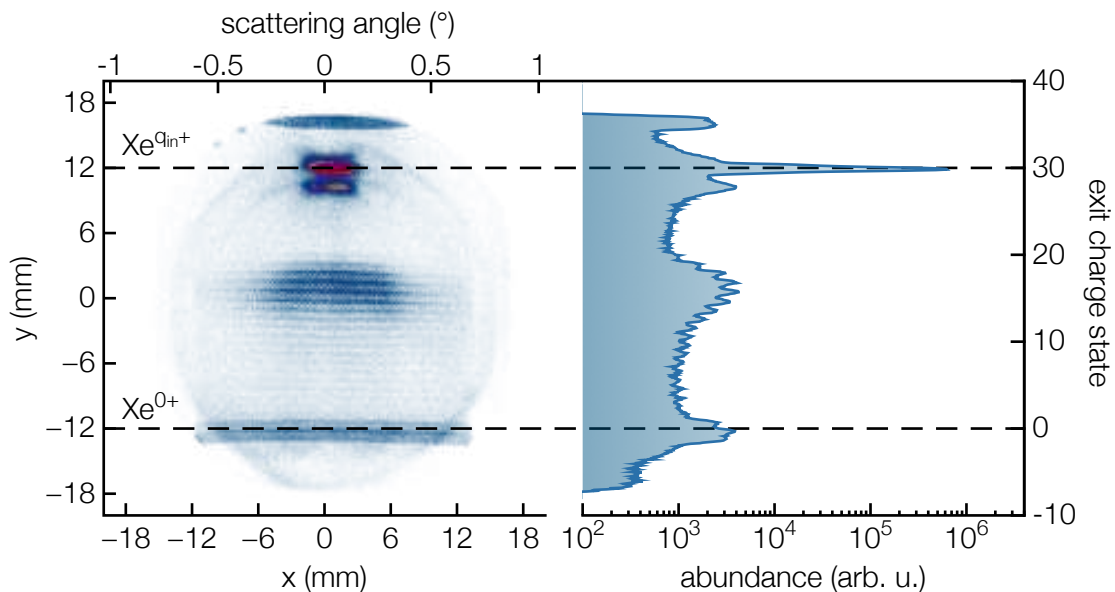

Figure 2.9: 2D map showing the exit charge state analysis as measured at the MCP detector. Conversion from x to scattering angle and y to exit charge state according to equations (2.5) and (2.4), respectively, is given on the upper and right axis. The right graph shows the projection of recorded counts on the y and exit charge state axis.

Time of flight measurements and filtering

Impinging particles on the MCP also provide a timing signal which together with the electron emission statistics pulse can be used for the determination of the time of flight (TOF) of ions transmitted through a sample.
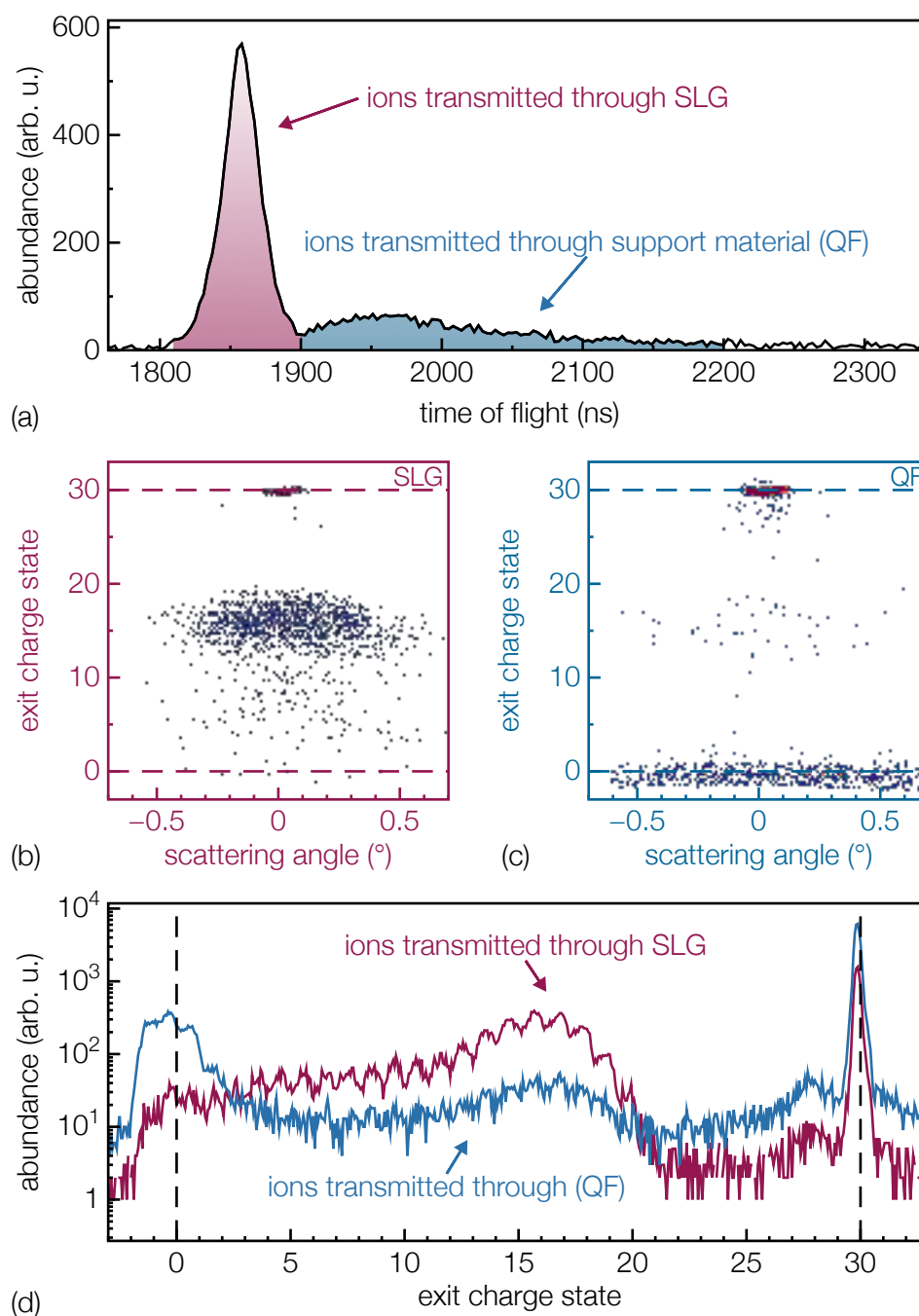
Figure 2.10: (a) Time of flight spectrum of 146 keV Xe^{30+} transmitted through SLG. The red coloured peak represents ions transmitted through SLG whereas the blue distribution arises from ions transmitted through QF. (b) and (c) 2D maps showing only counts with TOFs in the red or blue distribution in (a), respectively (cf. figure 2.9). (d) Exit charge state projection of spectra (b) and (c).

Figure 2.10 (a) shows a typical TOF spectrum for 146 keV Xe^{30+} transmitted through a single layer graphene sample composed as shown in figure 2.3. A distinct TOF peak belongs to ions transmitted through graphene, whereas a broad distribution represents ions transmitted through the support material (e.g. Quantifoil + 50 nm Au). The corresponding 2D spectrum can be seen in figure 2.9.

Given the way of measuring time of flight via emitted electrons as one trigger signal, ions transmitted through holes should not produce TOF events. This is however not the case as primary ions are detected at any time due to random coincidence producing TOFs at all values.

It is now possible to filter 2D spectra to show only counts with corresponding TOFs in a specific window. In figure 2.10 (b) and (c) there are spectra showing only counts with TOFs in the SLG and the QF region, respectively. It is notable that ions transmitted through support material have lower (close to or even neutral) exit charge states than ions transmitted through a single layer of graphene, which is in agreement with a thicker sample and hence a longer interaction time for the ion to capture and stabilise electrons. Projections of both 2D maps on the exit charge state axis are compared in figure 2.10. Due to the above mentioned accidental coincidental counts, primary ions are seen even in TOF filtered spectra.

2.3 Beam energy distribution

For some experiments it is crucial to know the energy distribution of the extracted beam from the ion source. We defined the energy distribution of our setup in two ways which are described below. Experiments therefore were also performed using argon as working gas besides xenon.

Method 1: retarding field analysis at the start of the beamline

First, we measured the beam current on a plate right at the entrance to the target chamber. Applying a retarding field to this slit leads to a decrease in current if the retarding field equals the energy of the beam. Since the beam energy distribution follows a Gaussian profile, the current decrease can be described as an error function

$$f(E) = a \cdot erf\left(b(x - x_0)\right) + c. \tag{2.6}$$

The full width at half maximum (FWHM) of the derivative Gauss function then describes the energy distribution of the ion beam (cf. figure 2.11).

Nevertheless, for various U_b, the resulting data of Xe^{11+} needs to be fitted by the superposition of two error functions as in equation (2.6) leading to the conclusion that there are two energy distributions extracted from the ion source. Experimental data and fits are shown in figure 2.12 (a) and (b).
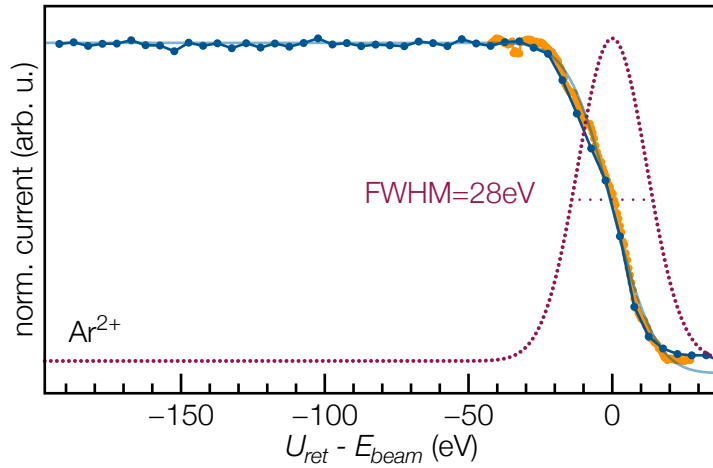
Figure 2.11: Retarding field analysis of beam energy distribution measured at a plate at the beginning of the target chamber right after the beam is extracted from the ion source.
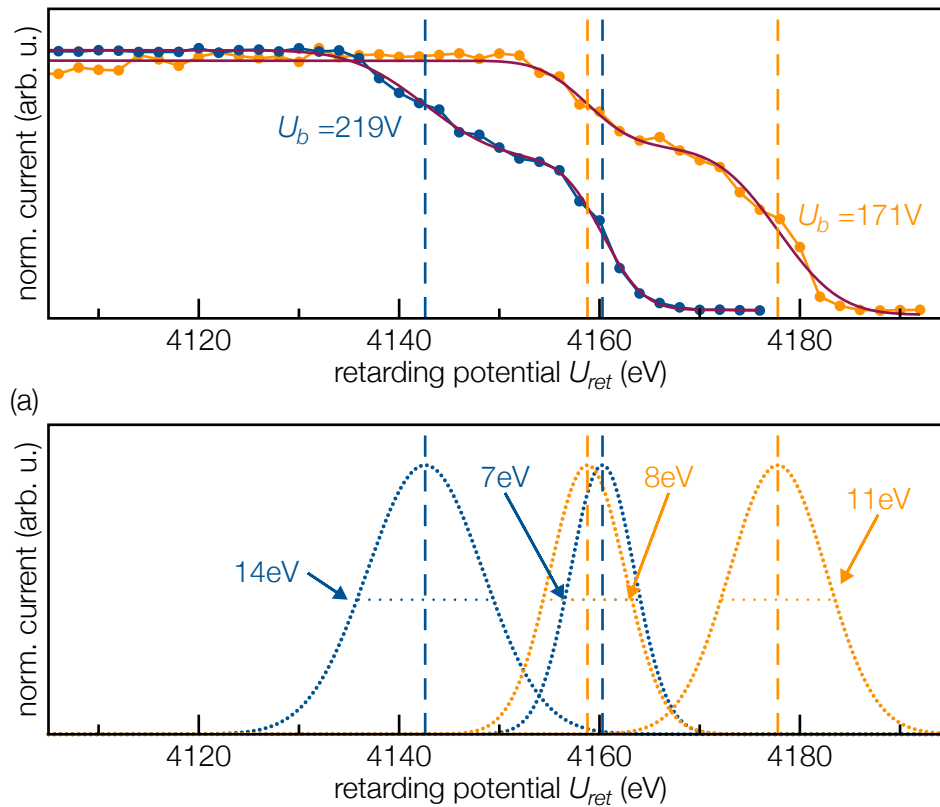

(a)

Figure 2.12: Retarding field analysis of the beam energy distribution: (a) instead of one error function, a superposition of two needs to be fitted to experimental data suggesting that there are two energy distributions extracted from the ion source. Measurements were done using Xe^{11+}, $U_0 = 4500\,V$ and $U_a = 300\,V$. (b) differentiating the fitted error function yields the FWHM of the energy distributions.

The origin of this feature is yet unclear. It may be that ions are created at different places in the ion source and hence extracted with slightly different energies. Otherwise, it is also possible that there is a geometric effect involved leading to minor differences in deceleration behaviour.

The final beam width derives from a combination of effects such as different origins inside the source. The Wien filter also has an energy window of ± 15 eV which leads to an energy dispersion. Slits inside the chamber allow to reduce the energy spread of the ion beam measured after exiting the ion source. The second method focuses on the determination of the energy distribution at the end of the chamber after the ions have passed various slits.

Method 2: beam deflection in deflection plates at the end of beamline

To measure the beam energy distribution at the end of the chamber we recorded various MCP spectra for constant beam settings and diversely biased deflection plates to study the broadening of the beam due to the presence of various ion energies and hence different deflection.
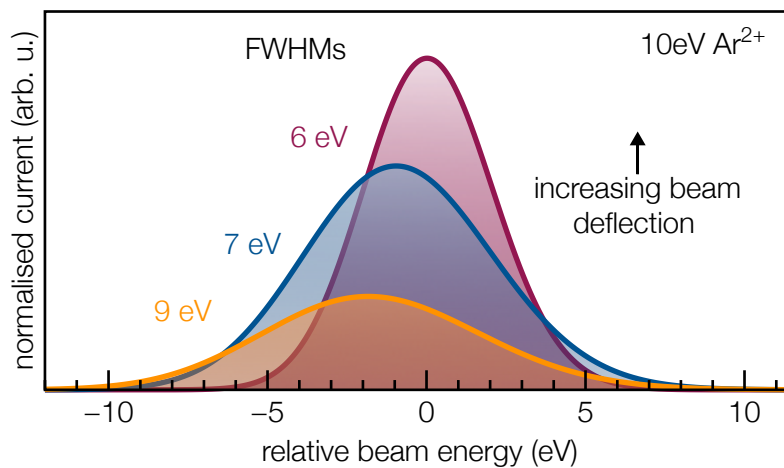

Figure 2.13: Beam energy distribution - analysis via deflection plates.

Since the width of the beam on the MCP is a convolution of the energy distribution originating from the source f and the slits used to cut the window g, $f * g$, transformation of the convolution theorem

$$\mathcal{F}(f * g) = \mathcal{F}(f) \cdot \mathcal{F}(g) \tag{2.7}$$

is possible to derive f after measuring $f * g$ and g (width of the beam without applied bias). By means of our measurement, we first derive the Gaussian form of f in dependence of y

$$f(y) = e^{-a(y+b)^2}, \tag{2.8}$$

27

which we can then transform into a dependence of E via equation (2.3) to

$$f(E) = f(y(E)) \cdot \frac{\mathrm{d}y}{\mathrm{d}E} = e^{-a\left(\frac{KU}{E}+b\right)^2} \cdot \frac{KU}{E^2}, \quad K = \frac{1}{2}\frac{q_{out} \cdot l}{d} \cdot \left(\frac{a}{2}+b\right). \tag{2.9}$$

Final results for $10\,\mathrm{eV}$ Ar^{2+} are presented in figure 2.13 showing a beam energy distribution of approximately $10\,\mathrm{eV}$.

Still, the energy width depends on the charge states of the ions and is in general higher for less charged ions, because of different extraction possibilities within the ion source. The origin position of highly charged ions is better defined due to enhanced trapping at higher q. Based on the retarding field method the energy width is determined to be below $15\,\mathrm{eV}$ for highly charged ions.

3 Discussion and results

The following chapter summarises results produced during the work for this thesis. In the beginning, two technical sections present changes in our measurements after heating either with a heating wire or with laser annealing. Afterwards, results from cleaned SLG samples are compared to previous data whereas data for trilayer graphene is added for comparison. The cleanest state achievable with our technical possibilities is further on denoted as clean even though I am aware that it is possible that the reached cleanliness might still be improved via other techniques.

3.1 Heat treatment

As described in section 2.2, the sample holder containing up to three TEM grids can be heated using a 1Ncl15 heating wire. Heating up the target holder however takes some time, because of an increase in the target chamber pressure. Figure 3.1 shows the time dependent temperature (measured with a PT1000 temperature element) and target chamber pressure during the first heat up. Without concern of a momentary large pressure increase ($\sim 5 \cdot 10^{-7}$ mbar) up to 380°C can be achieved within a day.
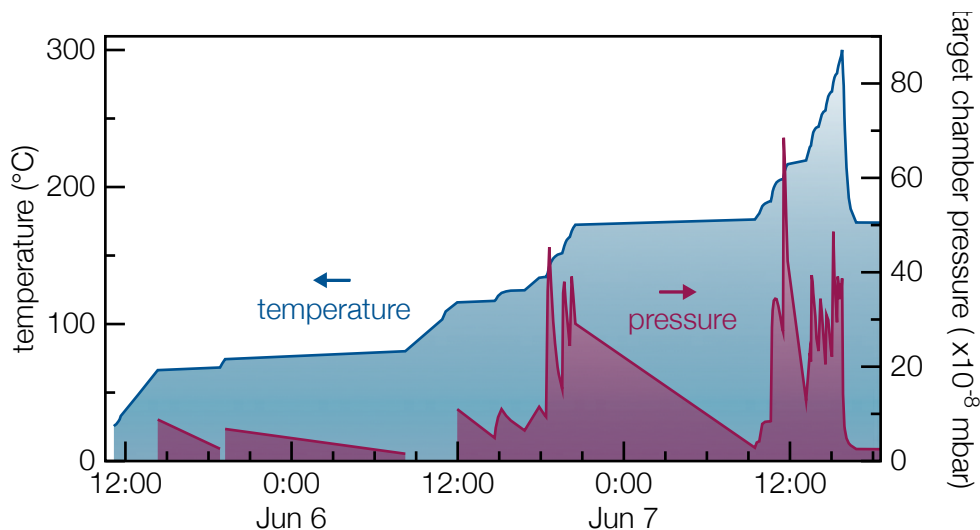

Figure 3.1: Temperature (blue) measured via a PT1000 heating element and target chamber pressure (red) during the first heat up. An increase in the target pressure can be seen with every increase in temperature.

29

For every current, an equilibrium temperature exists which is reached at the target holder after a certain time of heating. Table 3.1 as well as figure 3.2 (a) show this relation of heater current and equilibrium temperature, which can be used to adjust the setup to a desired temperature.

Table 3.1: Equilibrium temperature T for various heater currents I.

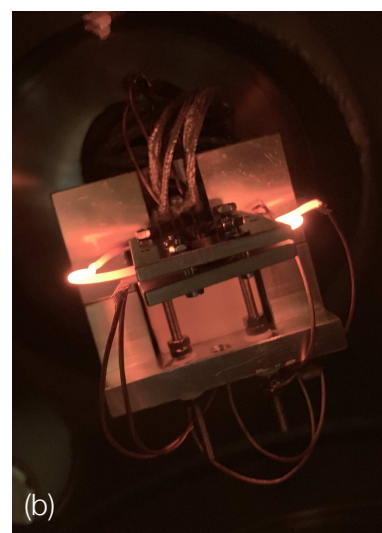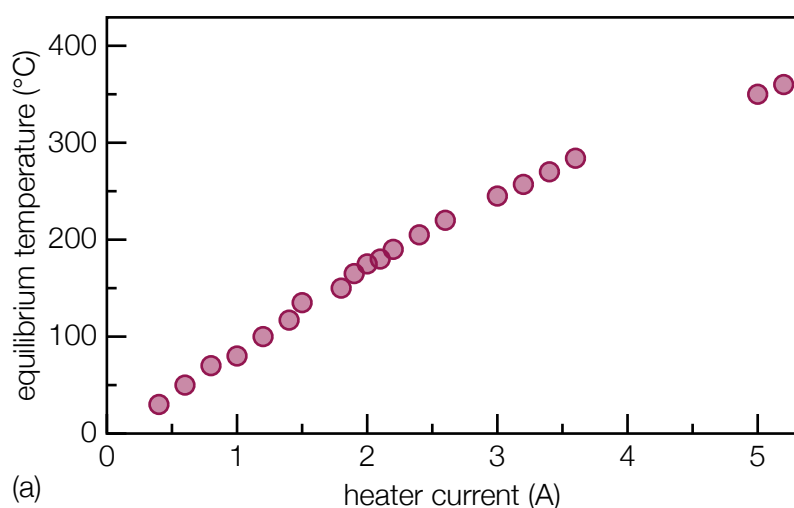| I (A)	T (°C)	I (A)	T (°C)
0.4	30	2.1	180
0.6	50	2.2	190
0.8	70	2.4	205
1.0	80	2.6	220
1.2	100	3.0	245
1.4	117	3.2	257
1.5	135	3.4	270
1.8	150	3.6	284
1.9	165	5.0	350
2.0	175	5.2	360

Figure 3.2: (a) Equilibrium temperature for various heater currents. (b) After roughly 250°C, the heating wire starts to visibly glow which might be the reason for more background noise and thus less efficient time of flight measurements.

This heating method allows to simultaneously measure and to study the development of our spectra. Nevertheless, either the pressure increase or background signals due to emitted radiation and light (see figure 3.2 (b)) makes evaluation of TOF as well as 2D spectra difficult. Hence, I could only observe changes for $T < 250$°C and again the whole temperature range while cooling. I reach ~ 380°C as maximum temperature.

Figure 3.3 shows results from the transmission of 146 keV Xe^{30+} through single layer graphene. From the beginning of the first heat treatment, a slight increase in the exit charge state and a

decrease in the time of flight is noticeable. There is a jump in both observables between 250°C and 350°C (in this region we could not perform measurements due to too much noise on the PIPS detector).
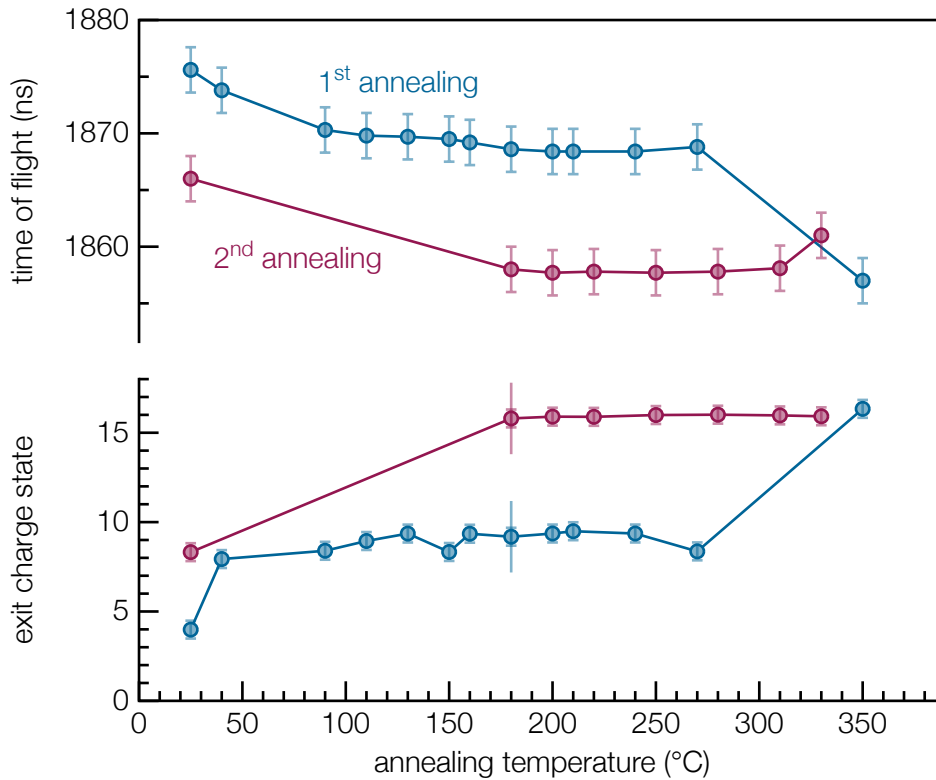

Figure 3.3: Time of flight (above) and exit charge state (below) versus temperature for 146 keV Xe^{30+} transmitted through SLG. Initial annealing (blue) shows minor decrease (increase) in time of flight (exit charge state) for $T \sim 150$°C and a rapid change between 250°C and 350°C. A second annealing process (red) already reaches the final values from the first annealing for both measurands at $T \sim 180$°C. The line added to one exit charge state data point describes a possible systematic error applicable to all data points in the same way.

Because of our target chamber pressure of $\sim 1 \cdot 10^{-8}$ mbar our samples get measurably contaminated again within the duration of one night. This is shown in figure 3.3: comparing the blue data point (first annealing) at 350°C and the red data point (second annealing) at 30°C shows a decrease in the exit charge state of 146 keV Xe^{30+} transmitted through SLG by 8 captured electrons. Similar behaviour can be observed in the time of flight spectrum. However, when heating the sample again only ~ 180°C are necessary to reach the previous highest possible exit charge state again. This manner does not even change when samples are exposed to air and remounted inside the chamber.

I explain this as follows: in the beginning, contaminations on the sample are made up of PMMA

or other residuals from production and transfer on the TEM grids in addition to always present hydrocarbons (cf. section 1.2). Latter ones seem to desorb at lower temperatures seen in the slight change in the beginning of the heat up. PMMA is cleaned only at higher temperatures (consistent with [57]) leading to the sudden change at temperatures between 250°C and 350°C in both spectra. Afterwards, at room temperature only hydrocarbons are adsorbed on the sample again, resulting in a lower temperature needed to clean the sample again.

STEM was then employed to gather information on the level of contamination of our samples. Figure 3.4 shows one spot on one heated SLG sample.
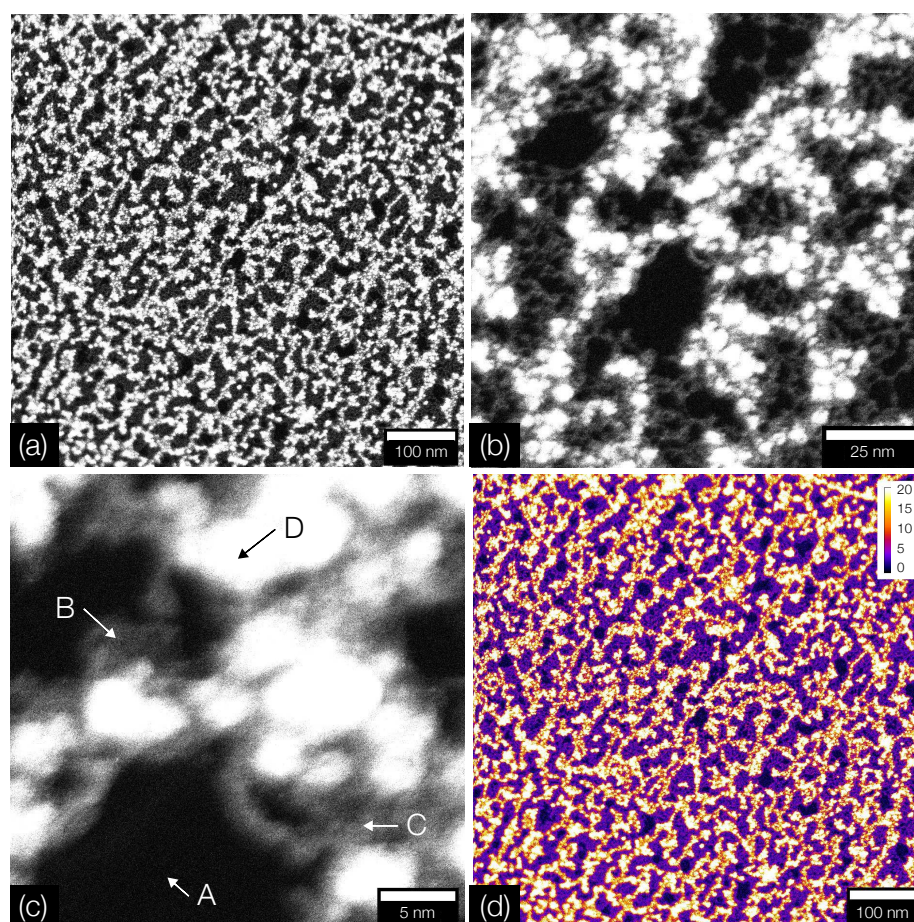

Figure 3.4: STEM images of annealed SLG. (a) - (c) show various spot sizes. Scale bars are denoted in the lower right corner. Labels in (c) are explained in the text. (d) is a coloured version of (a) presenting the equivalent sample thickness in number of graphene layers (colour scale in upper right corner).

Whereas pictures (a)-(c) show different spot sizes (as denoted in scale bars in the lower right corner), figure (d) is a coloured version of (a). There, the colour scale in the upper right corner presents an equivalent thickness in number of graphene layers enabling the characterisation of spots labelled in picture (c):

A clean spots of single layer graphene

B regions with hydrocarbon adsorbates surrounding clean areas (equivalent thickness 4-5 monolayers)

C hydrocarbon adsorbates (equivalent thickness < 10 monolayers)

D heavy/thick residuals (equivalent thickness 20-70 monolayers) in the form of clusters

To characterise the heavy/thick residuals marked as D in figure 3.4, energy-dispersive x-ray spectroscopy (EDX) was performed. The two measured samples with similar STEM results show a high amount of gold. Since only one of the samples has a Au coated (50 nm) Quantifoil and analysed spots were not close to the Au TEM grid, the origin of this Au amount is yet unclear. This could possibly stem from background of the TEM grid or diffusion of Au atoms. So, EDX did not yield a satisfying characterisation of detected contamination.

Altogether, heating the target holder with the heating wire was used for single layer and trilayer graphene (TLG) samples (cf. figure 3.5).
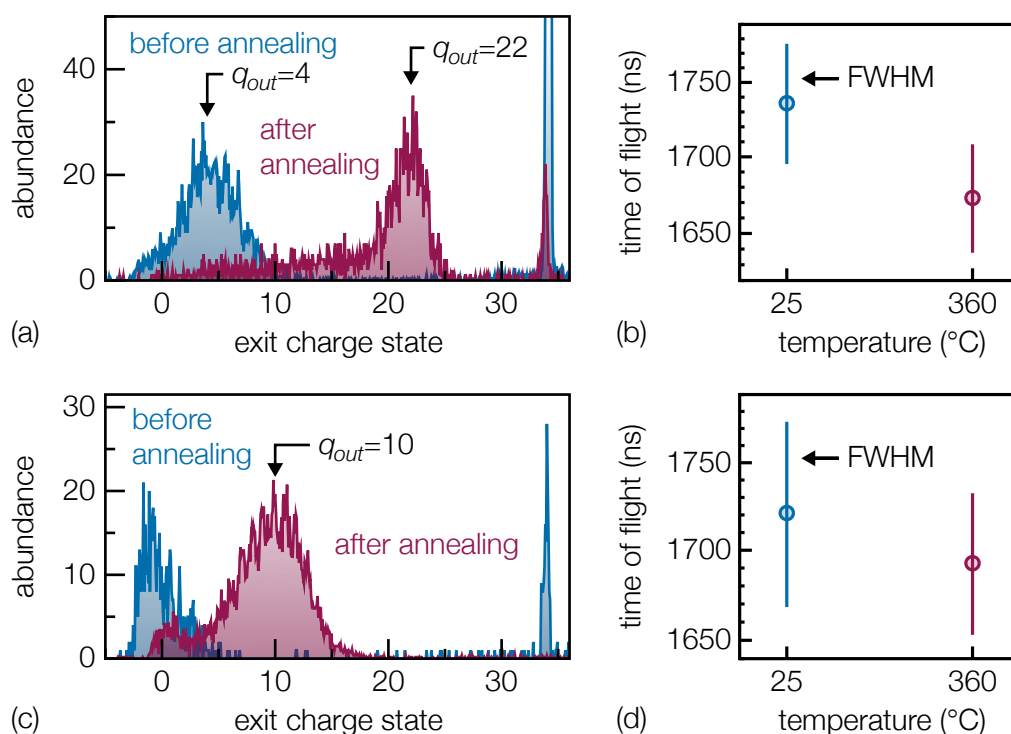

Figure 3.5: Annealing of SLG (a)-(b) and TLG (c)-(d): exit charge state (a,c) and TOF (b,d) spectra are given before (blue) and after (red) annealing at $T = 360°C$. The added line in the time of flight spectra represent the width of the TOF peak indicating its narrowing during heating.

Either of them show substantial shifts both in the exit charge state (to higher values) as well as

in time of flight (to shorter times).

3.2 Laser treatment

To try another way of cleaning the sample, a Lasertack 6 W 445 nm laser diode [78] was installed at our setup. The laser can be controlled via a modulation voltage U_{mod} between 0 and 5 V, which changes its output power. The smallest spotsize achievable is 4x1 mm. In our setup we used a 5x3 mm spot and not full laser power. However, future plans involve revision of this setup and exact determination of the laser power and power density.

Before the laser can be used for systematic cleaning procedures, it is crucial to understand its functioning in regard to necessary modulation voltage and needed duration of operation for cleaning. Measurements performed to clarify these question are described in the following.
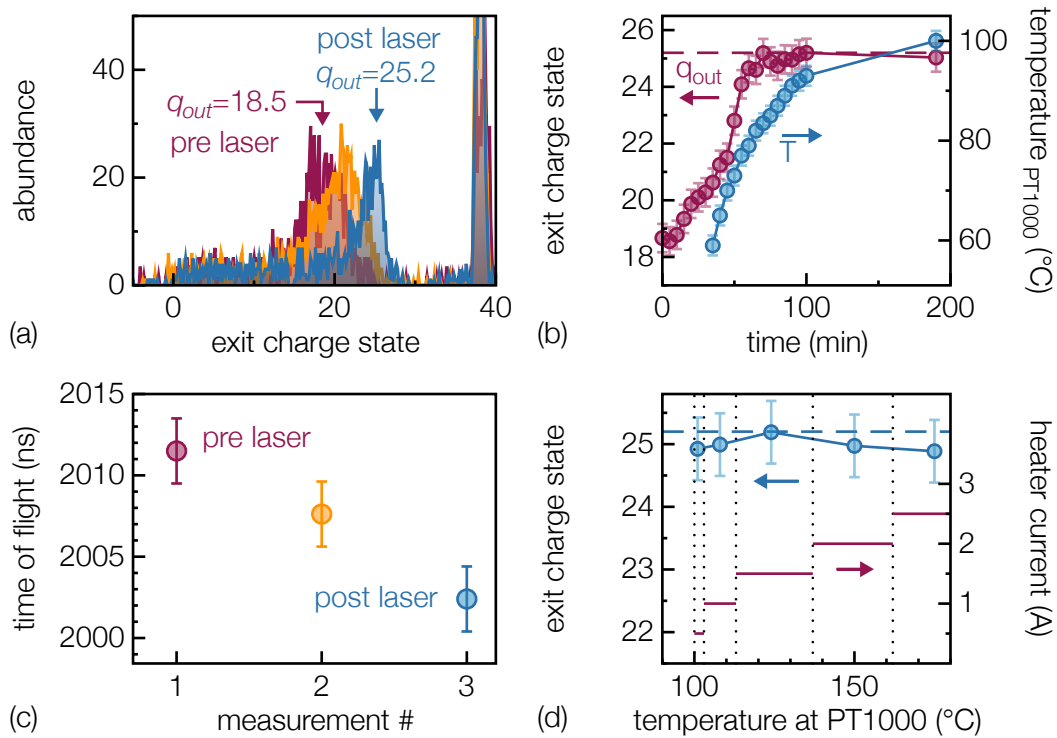

Figure 3.6: Laser annealing of SLG (170 keV Xe^{38+}): (a) q_{out} spectra before (red), 30 min after beginning (orange) and after one hour (blue) of laser operation with U_{mod}=3.5 V. (b) q_{out} (red) and target holder temperature (blue) vs. time. The laser was operated at U_{mod}=5 V. A clean sample is reached after approximately one hour. (c) The shift in q_{out} in (a) is again accompanied by a decrease in TOF. (d) Additional heating using the heating wire described in section 3.1 while irradiating the sample with our maximum laser power does not further change q_{out}.

First, I increased the modulation voltage in steps of 0.5 V (approximately 30-60 minutes operation time between steps) and monitored the exit charge state of 170 keV Xe^{38+} transmitted through a single layer of graphene. We observed small changes in q_{out} and TOF rather quickly, although major changes occurred at 70% of our maximum laser power (cf. figure 3.6 (a) and (c)).

Figure 3.6 (c) shows the corresponding time of flight spectra to the exit charge distributions shown in graph (a). Similar to (a), the values change continuously within approximately one hour.

Furthermore I investigated the amount of time needed to clean the sample while using the laser at its maximum power. In order to do so, the sample was left to be contaminated in our vacuum chamber for one night. Figure 3.6 (b) depicts q_{out} and T in dependence of time, $t = 0$ marks the start of laser operation at full power. A cleaned sample was observed after ~ 1 hour. The PT1000 was placed approximately 15 mm next to the spot the laser was focused to. Since a similar behaviour as with the heating wire was detected, we conclude that the cleaning processes are also thermally driven.

On top of the laser at full power, I used the heating wire to check whether q_{out} and TOF shift further at higher temperatures. No further change can be observed neither during nor after heating the sample holder to $\sim 400°$C. Measured q_{out} until a heater current of 2.5 A are depicted in figure 3.6 (d).

Further cleaning procedures of other samples showed that the laser was not perfectly focused onto the sample position before. With a focused laser beam I am now able to clean our samples within seconds rather than over hours. The correctly aligned setup was used for all described measurements using the laser later on.

Single layer graphene

Cleaning a virgin SLG sample (provided by Graphenea [51]) brought information on the amount of contamination on the sample before cleaning.

Before laser treatment only one TOF peak was visible (shown in blue in figure 3.7). After turning on the laser two peaks emerged (red): ions transmitted through SLG (left peak, shorter TOFs) and ions transmitted through Quantifoil (right distribution, longer TOFs). Fitting the QF distribution with TRIM [82] (170 keV Xe through 10 nm carbon) enables coarse estimation of contamination thickness. Using TRIM results and assuming a linear energy decrease with material/contamination thickness yields the contamination thickness scale on top of figure 3.7. This suggests that there are ~ 2 nm contamination on virgin samples (taking carbon as main component). A Moyal distribution was used to fit simulated data:

$$f(x) = a \cdot e^{\left(\frac{x-x_0}{2\sigma} - \frac{1}{2}e^{\frac{x-x_0}{\sigma}}\right)}$$
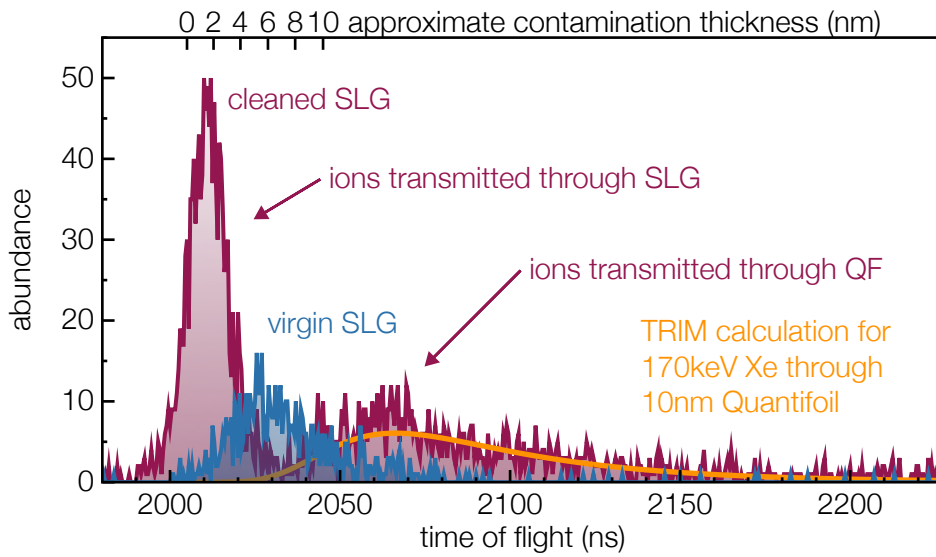
<div align="right">(3.1)</div>

Figure 3.7: TOF spectra for virgin (blue) and cleaned (red) SLG. Fitting (orange line) the QF TOF distribution via TRIM calculations results in a contamination thickness of $\sim 2-3\,$nm. 170 keV Xe^{38+} was used as projectile.
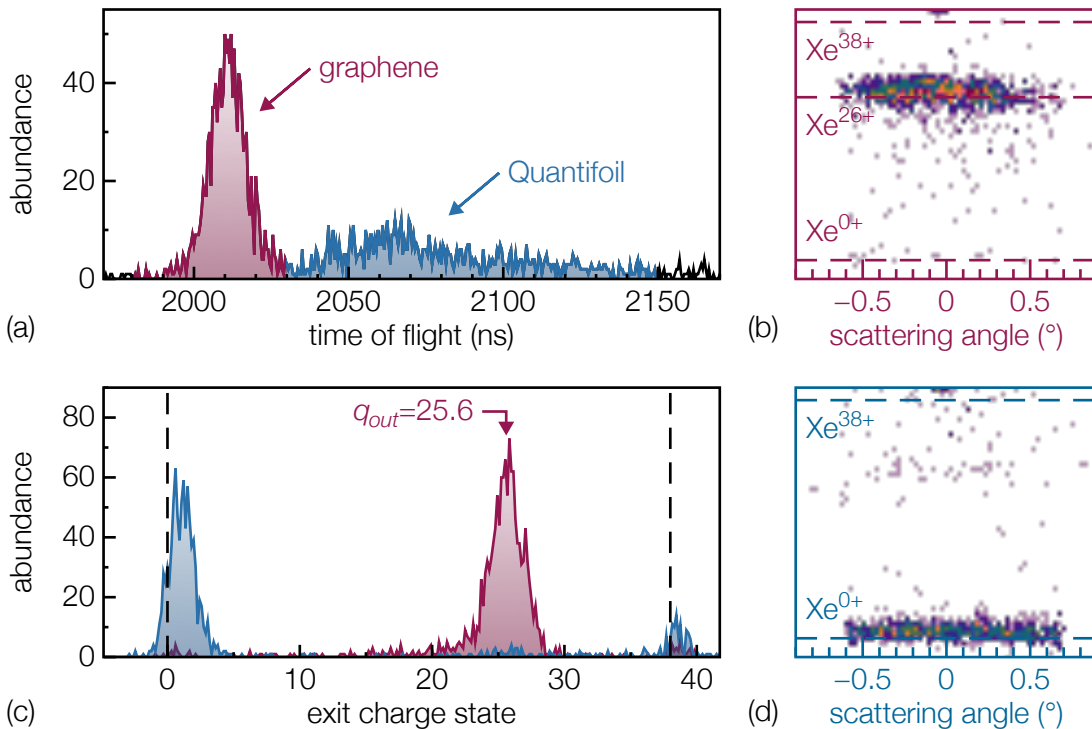

Figure 3.8: (a) Separation of the SLG TOF peak into ions transmitted through SLG and QF (170 keV Xe^{38+}). (b) and (d) show TOF filtered 2D spectra for graphene and Quantifoil, whereas (c) shows the corresponding exit charge state projections.

TOF filtering for graphene and Quantifoil at the clean sample shows neutralised Xe after transmission through QF and an exit charge state distribution around $q_{out} = 25.6$ for ions transmitted through a single layer of graphene. The TOF spectrum and filtered 2D maps as well as exit charge state distributions are presented in figure 3.8. All spectra are colour coded with regard to the coloured TOF spectrum in graph (a).

Bilayer graphene

As shown for single layer graphene in the previous part, the time of flight spectrum of 170 keV Xe^{38+} also separates into ions transmitted through bilayer graphene (BLG) and Quantifoil, respectively. Again, TOF spectrum, TOF filtered 2D maps and exit charge state distributions are shown in figure 3.9.
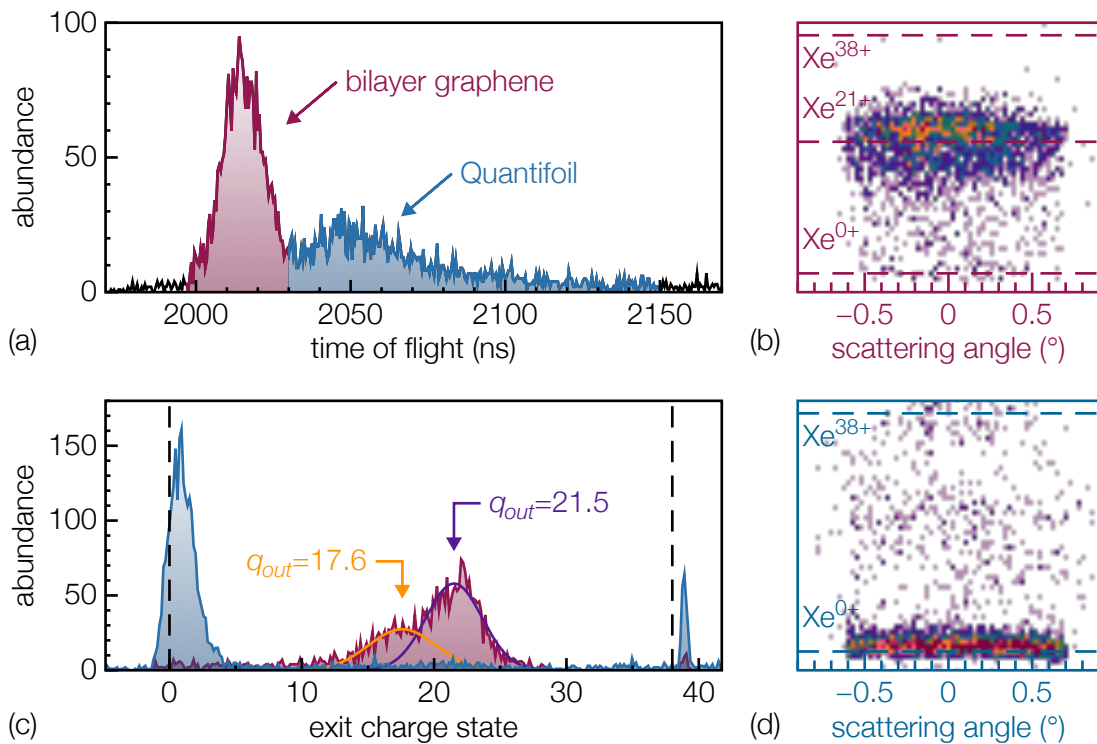

Figure 3.9: (a) Separation of the BLG TOF peak into ions transmitted through BLG and QF, respectively. (b) and (d) show the TOF filtered 2D spectra for bilayer graphene and Quantifoil, whereas (c) shows the corresponding exit charge state distributions. In graph (c), a second charge state distribution can be seen (orange), probably belonging to areas either still covered with contamination or hosting a third layer of graphene. 170 keV Xe^{38+} was used as projectile.

In figure 3.9 (c) a second distribution (orange) can observed for cleaned bilayer graphene, which possibly arises from either areas on the sample covered with a third graphene layer or ones that are still contaminated.

The next step was to see how fast our samples get contaminated again after having been cleaned. So hourly measurements were recorded after turning the laser off. In figure 3.10 it can be seen that both exit charge state and TOF keep close to its optimum value for approximately 7-8 hours before rapidly dropping/increasing before evening out after ~ 15 hours.

This is unexpected and can be partially explained by the fact that the sample first needs to cool down before contaminations can be adsorbed again. Previous measurements conclude that cooling takes approximately 2 hours which therefore does not fully explain the reported behaviour.
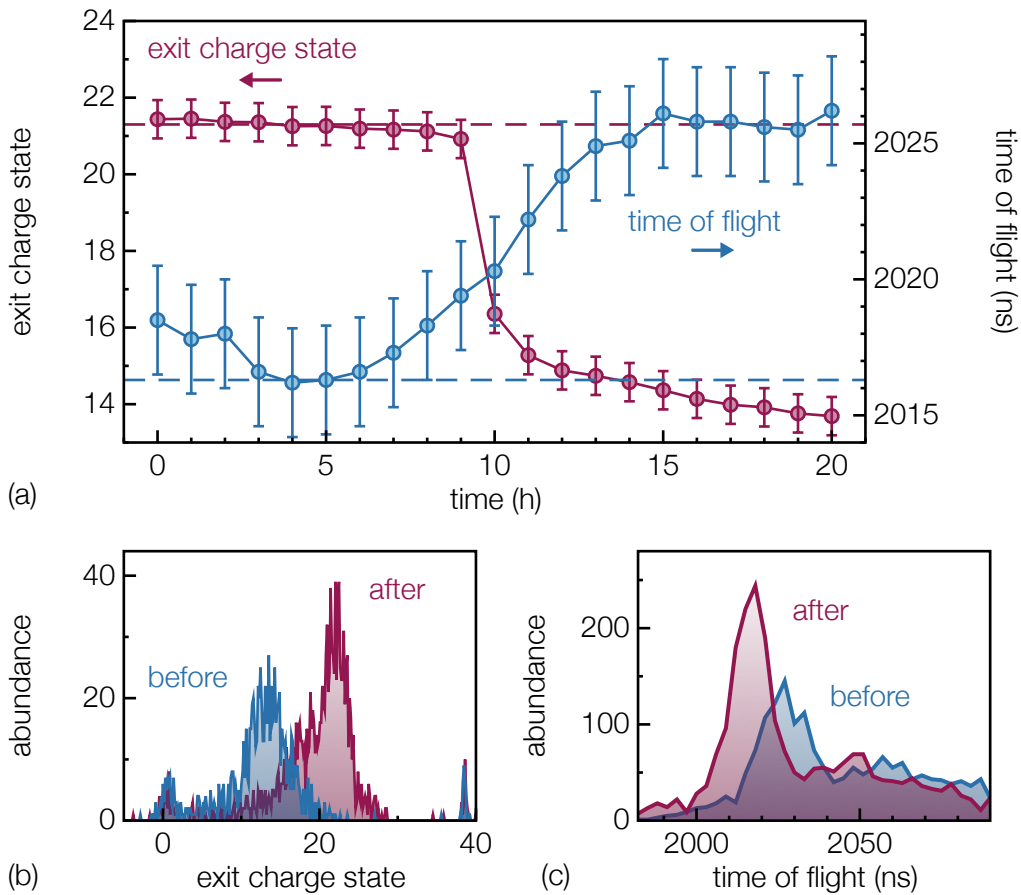
Figure 3.10: (a) Within one night without cleaning the samples are being contaminated again. After staying clean for a few hours the exit charge state drops rapidly which is first observable in the measurement at $t = 10\,$h. A continuous increase in TOF starts earlier. (b) and (c) After the measurement series depicted in (a) q_{out} (b) and TOF (c) were measured for five minutes before (blue) and after (red) the laser was turned on again. $170\,$keV Xe^{38+} was used as projectile.

Since in figure 3.10 (b) and (c) the measurement after turning on the laser (red) shows an immediately cleaned sample compared to the contaminated sample (blue), we conclude that a correctly aligned laser cleans the sample within seconds. The poor statistics stems from a five

minute measurement time, which was used to emphasise the rapid cleaning.

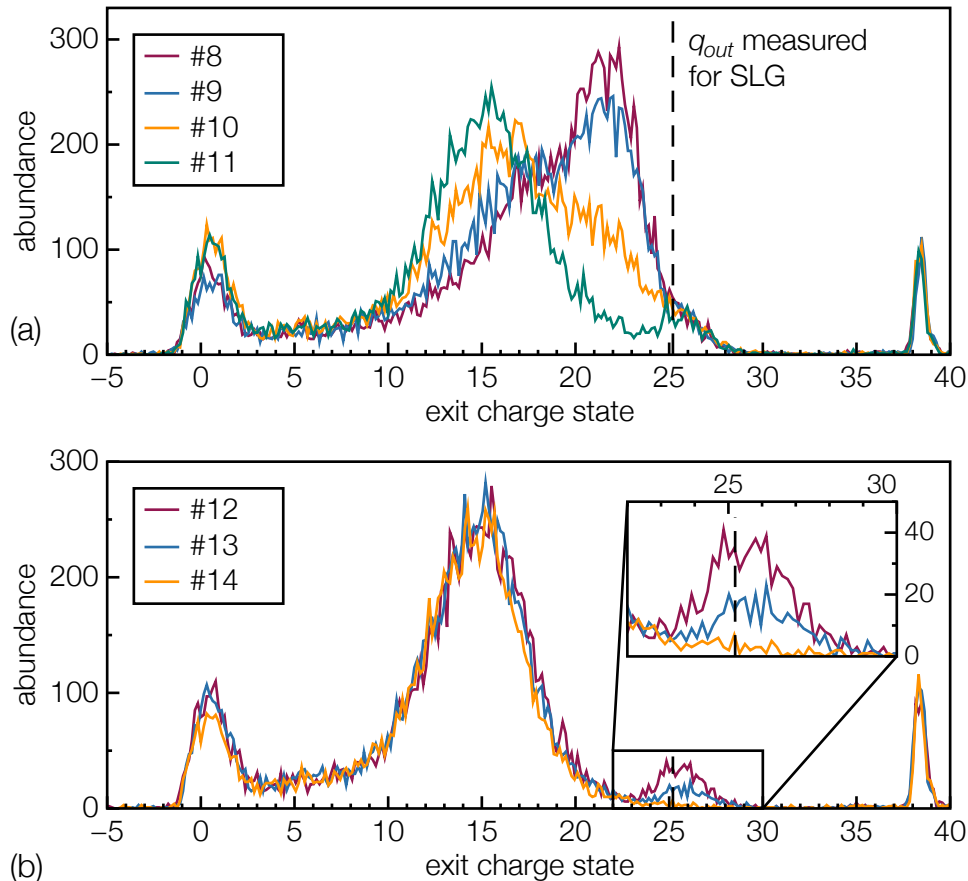Figure 3.11 shows exit charge state spectra of measurements number 8-14 from figure 3.10.

Figure 3.11: Measurements 8-11 (a) and 12-14 (b) of the measurement series plotted in figure 3.10. After the shift of the bilayer distribution to lower exit charge states, a second exit charge state distribution (merging with the BLG peak at lower values several hours later) emerges which can be associated with the single layer graphene fractions on the BLG sample. Measurements were recorded using 170 keV Xe^{38+} as projectile.

Within those hours the majority of change occurred. Closer examination of these measurements shows that after the BLG exit charge state distribution shifted to its lower value, a small distribution remains (measurement at $t = 11$ h, green line in plot (a)): its q_{out} corresponds to the exit charge state measured for single layer graphene using the same projectile with a smaller abundance than the one arising from bilayer graphene. Filtering the TOF spectrum with this exit charge state distribution shows a small TOF peak with a time of flight associated with single layer graphene (cf. figure 3.12). From this we deduce that our sample also contains SLG spots which is not uncommon in multilayer graphene samples.

This SLG distribution vanishes within the following 3 hours. Since this happens after BLG gets

contaminated it appears that the single layer fraction contaminates slower than the bilayer one. This is not explicable until now and further measurements will have to be made to reproduce and understand this effect.
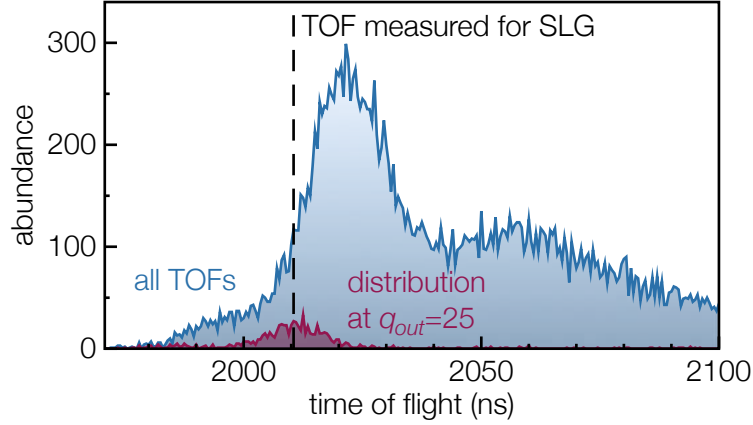

Figure 3.12: Filtered TOF spectrum using the supposedly SLG exit charge state distribution from figure 3.11. The resulting TOF peak matches the TOF peak measured with 170 keV Xe^{38+} transmitted through SLG emphasising this SLG character.

In figure 3.13 (a) a TOF distribution of particles arriving 24 ns before primary ions transmitted through single layer (and bilayer) graphene can be observed. A possible explanation could be forward sputtered C from our sample. The maximum energy transferred from Xe to (forward) sputtered C can be computed as follows:

$$E_C = \gamma \cdot E_{Xe} \tag{3.2}$$

$$\gamma = \frac{4m_1 m_2}{(m_1 + m_2)^2} = 0.307 \tag{3.3}$$

Albeit, calculating the time of flight shows that sputted C would have a TOF of $\sim$1000 ns less than Xe which eliminates the possibility of attributing this fast TOF peak to C. Other possible contaminants such as O ($\sim$ 970 ns faster than Xe), Si ($\sim$ 870 ns faster than Xe) or Cu ($\sim$ 750 ns slower than Xe) are also ruled out. Those particles are deflected by the deflection plates in the same way as Xe$^{q_{out}}$ (cf. figure 3.13 (b)), sputtered particles are usually neutral.

Because of our setup to measure time of flight (see section 2.2) a difference in TOF might also stem from different flight times of emitted electrons. Those are attracted by grids and after that accelerated by $\sim$ 30 keV onto a PIPS detector. The flight time until reaching the grids may vary depending on energy and emittance angle of the electrons.

The two distinct TOF peaks shown in figure 3.13 (a) would however need two clear "regimes" of emitted electrons either varying in much longer trajectories or in higher energy. Additionally, it is
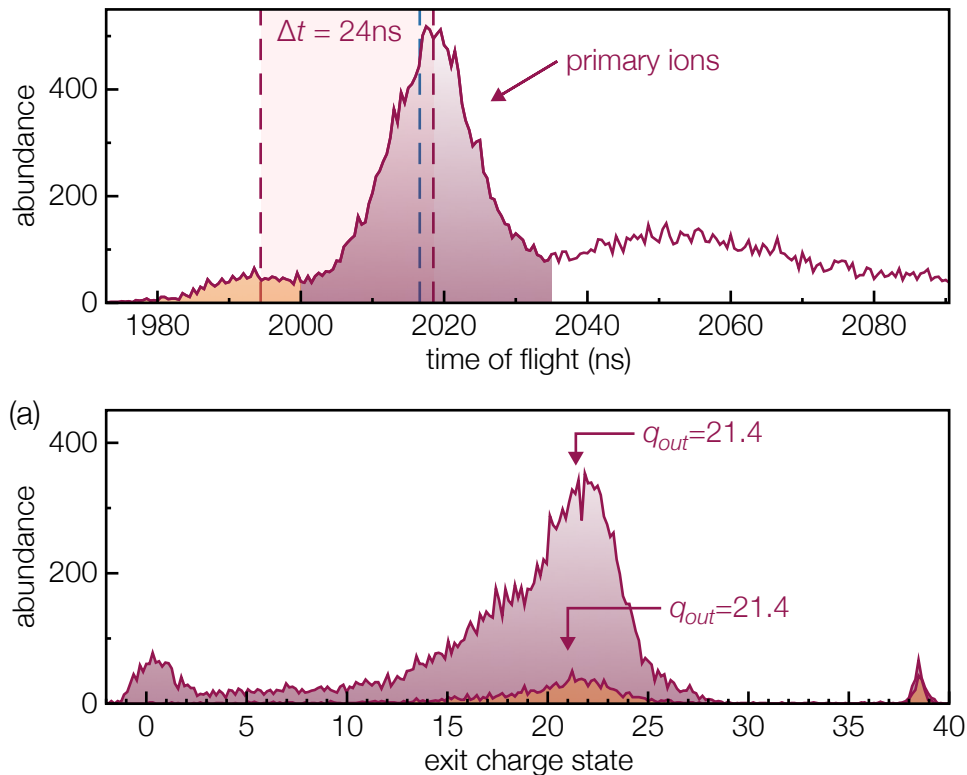
Figure 3.13: (a) TOF spectrum of 170 keV Xe^{38+} transmitted through bilayer graphene. A smaller second TOF peaks can be seen 24 ns before the TOF peak of ions transmitted through bilayer graphene, which has an even shorter TOF than the single layer fraction of the BLG sample (see figure 3.12). (b) The exit charge state distribution suits q_{out} measured with bilayer graphene.

not clear why this feature does not appear in any other spectra measured and presented before in this thesis. Even though, this would be an interesting point considering different neutralisation mechanisms (predicting also a variation in electron energy regimes) further measurements need to be conducted to confirm and study this behaviour. Also, the electron collection efficiency by the grids would need to be improved since simulations (cf. section 2.2) show a strong drop in collection efficiency for electrons with higher energies making measurements and especially comparison to electrons with lower energies increasingly difficult.

3.3 Comparison of single, bi- and trilayer graphene

Measurements using samples cleaned either by heating the sample holder via the heating wire or with the laser were performed using single, bi- and trilayer graphene samples all provided by Graphenea [51]. Results regarding the exit charge state, scattering of transmitted ions and neutralisation time of the projectile are discussed in this section.

Comparison to Gruber *et al.* **[61]**

Measured data for single layer graphene is compared to data published by Gruber *et al.* [61] in figure 3.14 where the mean number of captured electrons is given in dependence of $1/v$. Because annealed SLG was in general only used for higher velocities v, a direct comparison is only possible for one data point for Xe^{30+} with $1/v \sim 2\,(nm/fs)^{-1}$: There, I find that the mean number of captured electrons differs by ~ 6.5 electrons, i.e. in clean SLG less electrons are stabilised (ca. 67%) than in the experiment of [61].

Adding this data point also to figure 3.15 (Xe^{30+}) indicates that Gruber et al. used samples comparable to cleaned bilayer graphene thus approximately one layer of contamination.

New data points for higher velocities also lie below fits through data by Gruber *et al.* which is further discussed in the part "Neutralisation time" later on in this chapter.
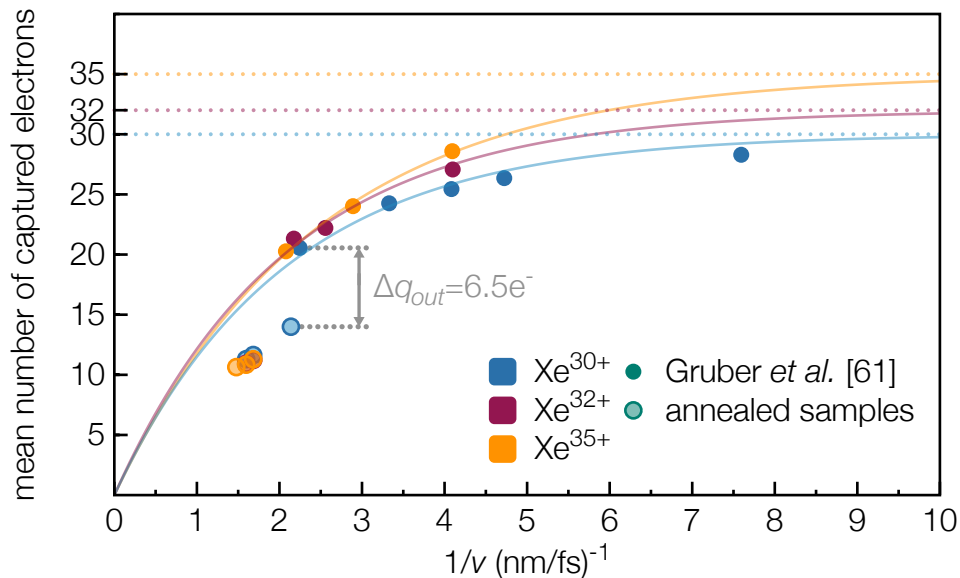

Figure 3.14: Data for SLG transmitted by various charge states and projectile energies given in dependence of $1/v$. Comparison between data published by Gruber *et al.* [61] and data from annealed samples is only possible for Xe^{30+} with $1/v \sim 2\,(nm/fs)^{-1}$ and shows a difference of ~ 6 electrons.

Charge exchange

All three samples were investigated with various charge states and also different ion energies. Figure 3.15 presents data points in dependence of the number of graphene layers for four incident charge states and up to three different energies.

To fit the data, additional points were considered for no captured electrons in case of no graphene layer $N_e(x = 0) = 0$ and q_{in} captured electrons for $x = 30$ graphene layers $N_e(x = 30) = q_{in}$. The latter one can be assumed since projectiles transmitted through Quantifoil ($\sim 10\,nm \sim 30$ graphene layers) are completely neutralised.
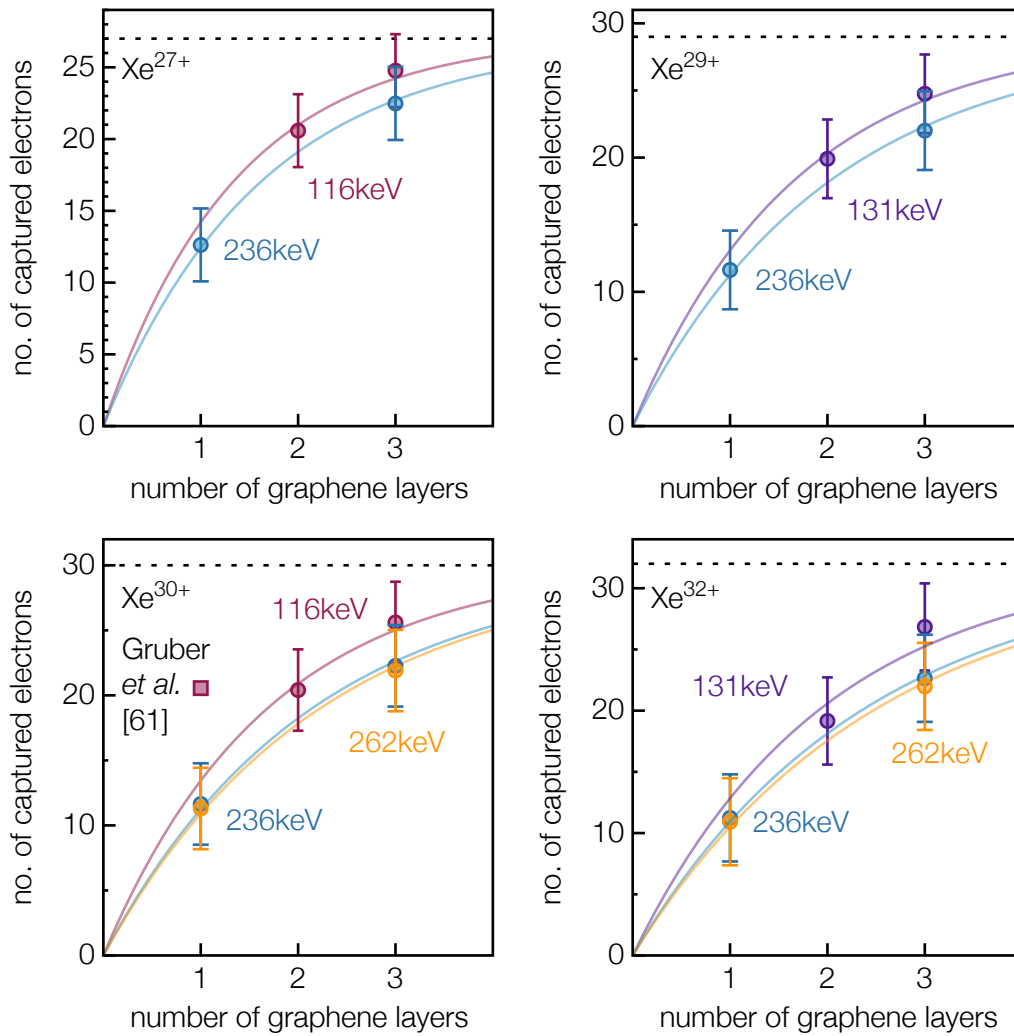
Figure 3.15: Number of captured electrons by $Xe^{q_{in}}$ with various energies for single, bi- and trilayer graphene in dependence of the number of graphene layers. Data points are fitted with an exponential behaviour (see text). Subfigures correspond to $q_{in}=\{27,29,30,32\}$. One data point from Gruber *et al.* [61] was added to the Xe^{30+} graph.

Then, the data can be fitted well using an exponential behaviour with only a single fitting parameter a:

$$N_e(\text{x}) = q_{in} \cdot \left(1 - e^{-\frac{x}{a}}\right)$$

(3.4)

The fitting parameter a describes a neutralisation length given in numbers of graphene layers and shows a linear dependence of the projectile energy in the examined energy region (cf. figure 3.15).

Figure 3.16: The fit parameter *a* from equation (3.4) describes the neutralisation length of xenon ions transmitted through SLG. A linear dependence with the projectile energy can be noticed.

Scattering measurements

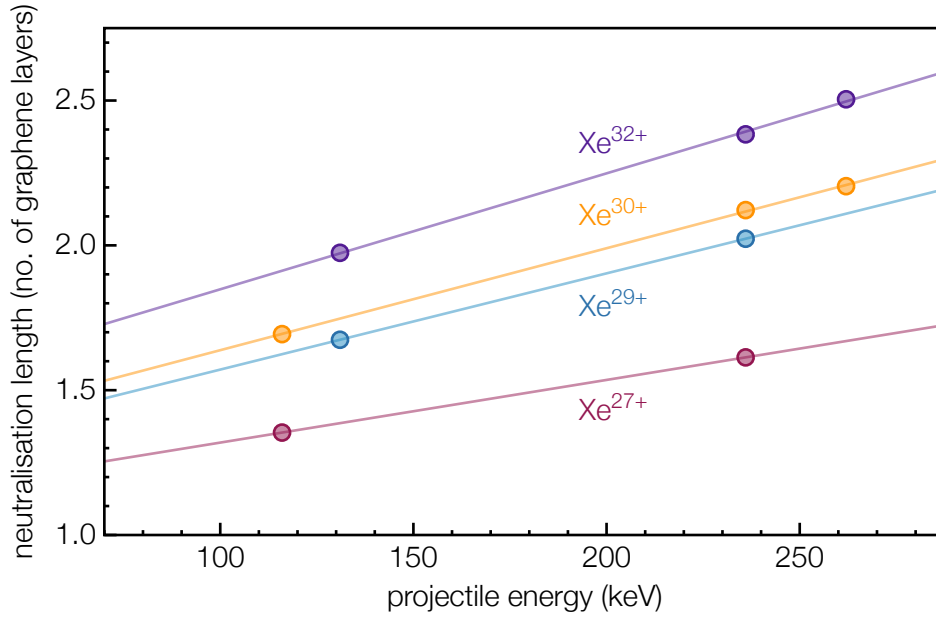In figure 3.17 scattering measurements for single, bi- and trilayer graphene are presented. Single layer graphene (a)-(b) and trilayer graphene (e)-(f) were measured with 166 keV Xe^{34+} whereas 170 keV Xe^{38+} was scattered at bilayer graphene (c)-(d).

For single layer graphene, projectiles can only collide with one target atom (assuming a contamination free sample and thus a thickness of only one atomic layer). Since the projectile mass m_1 is larger than the mass of target atoms m_2, there exists a maximum scattering angle φ_{max}:

$$\varphi_{max} = \arcsin\left(\frac{m_2}{m_1}\right) = 5.24° \tag{3.5}$$

For BLG and TLG multiple scattering becomes possible which can lead to a broader scattering distribution.

Since our MCP only detects particles scattered within an angle of $\pm 0.5\%$, rotating the TOF chamber and stitching together measurements is necessary to cover this angular sector. Because of instabilities of the ion source over the measurement durations of one hour per angle, stitching does not always work completely fine: for instance, regarding the TLG scattering 2D map (figure 3.17) shows cleary a higher intensity at positive angles. The projections of different measurements in graph (f) were scaled to match at the boundaries.

To compare those scattering distributions more easily, they are plotted one above the other in figure 3.18. While SLG shows a smaller peak width, there is no clear difference between

BLG and TLG. Still, 10 nm thick Quantifoil leads to higher scattering angles as can be seen in figure 3.17 (c) where the QF "stripe" on the MCP is still intense at angles where there are only few particles scattered by BLG left.
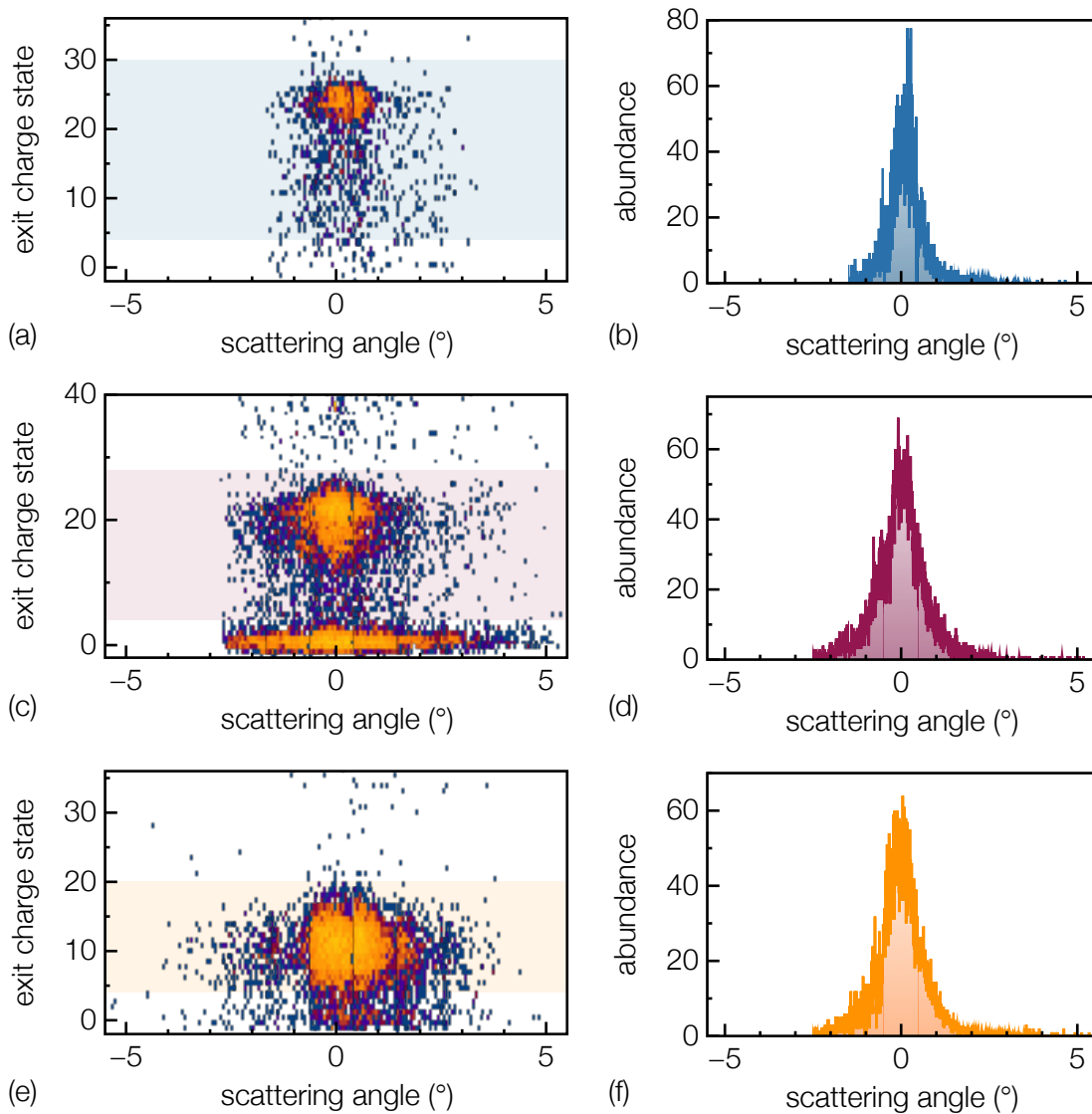

Figure 3.17: Scattering measurements of single (a)-(b), bi- (c)-(d) and trilayer (e)-(f) graphene. Spectra with single and trilayer graphene (cleaned via heating the target holder) were recorded with 166 keV Xe^{34+}, whereas the bilayer sample was laser cleaned and transmitted by 170 keV Xe^{38+}.
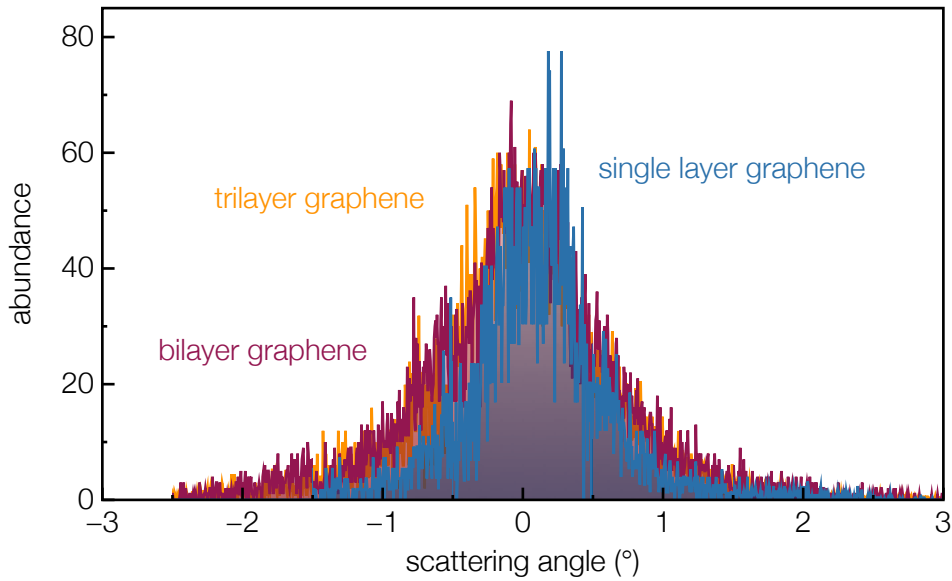
Figure 3.18: Comparison of scattering angles of ions transmitted through SLG, BLG and TLG. Whereas single layer scatters ions within a smaller angle area, there is no obvious difference in bilayer and trilayer spectra.

Neutralisation time

In section 1.3 figure 1.9 shows the number of captured electrons of Xe ions with various energies and incident charge states transmitted through single layer graphene. Adding data points from cleaned SLG samples primarily at high ion energies (thus short interaction times) however has great impact on this graph (cf. figure 3.19): a fit through the origin (zero captured and stabilised electrons at only zero interaction time) is no longer applicable. Instead, a second fit parameter needs to be used to introduce a finite velocity at which no charge exchange can occur. This may be explained by the picture that at some point, ions are too fast so that electrons cannot follow and thus no charge exchange appears any more.

For calculation of the interaction time, an effective target thickness consisting of the critical distance of the COB model modified by TDDFT calculations (equation (1.5)) is used. For BLG and TLG a third fit parameter adapting the effective interaction length (equation (1.5)) needs to be introduced:

$$d_{eff} = d_{eff_{SLG}} \cdot K \qquad (3.6)$$
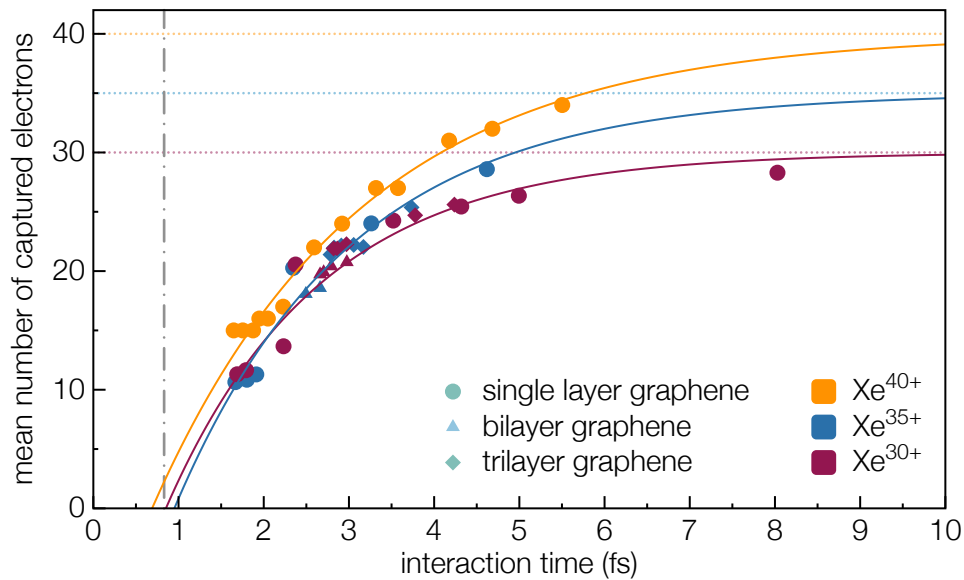
Figure 3.19: Mean number of captured electrons in dependence of the interaction time of $Xe^{q_{in}+}$ ions of various energies (cf. figure 1.9) complemented by additional data points for cleaned SLG, BLG and TLG samples. SLG data is fitted by the solid lines, BLG and TLG data is added via adjusting the interaction time with a relative effective thickness factor.

The best agreement was achieved using $K = 1.16$ for BLG and $K = 1.67$ for TLG. In case of TLG this would mean an increase by $\sim 6\,\text{Å}$, so two times the interlayer spacing of graphite which would correspond well to the trilayer nature of the sample. For BLG, $K = 1.16$ describes an increase in thickness by $\sim 1.5\,\text{Å}$ which cannot be interpreted as easily as for TLG.

4 Conclusion and outlook

Measurements presented in the previous chapter 3 have proven that samples show important changes after applying cleaning treatments. Annealing the samples via heating the target holder with a heating wire has thereby led to equivalent results as cleaning the sample with a 445 nm 6 W laser. However, laser cleaning has the advantage of not increasing the target chamber pressure which makes it easier to continue cleaning while recording spectra. Combination of both did not further change measured quantities such as the exit charge state distribution and time of flight of projectiles. This leads me to the conclusion that I already have achieved the cleanest state possible with our methods.

Laser cleaning does not (negatively) effect the target chamber pressure which also helps in regard to long-term measurements or irradiations. Measurements have shown that even at a base pressure of $4 \cdot 10^{-9}$ mbar (which seems to be the current optimum) the samples get contaminated again within less than ten hours without heat treatment.

Either treatment will be definitely used for future measurements to clean investigated samples. First spectra with cleaned samples were already recorded with single, bi- and trilayer graphene and used for comparison: the number of captured electrons shows an exponential behaviour regarding the dependence of the number of graphene layers. Scattering measurements indicate the scattering to higher angles of projectiles transmitting BLG and TLG compared to SLG samples. This is consistent with the fact that multiple scattering events (which become possible only starting with bilayer graphene) can lead to larger scattering angles than a single scattering process.

Additionally, analysing the number of captured electrons in dependence of the interaction time (as it was done in [19]) indicates the existence of a finite interaction time below which no charge exchange can take place.

However, there are also several open questions after having performed these measurements. The origin and nature of clustered residuals formed on graphene samples (maybe consisting of Au) is not understood to date. Also, the occurrence of a second time of flight peak in measurements with bilayer samples (cf. section 3.2) is inexplicable until now. Whether this peak consists of (sputtered) particles fitting to the measured time of flight or whether it comes from a high energy regime of emitted electrons needs to be investigated further to give more detailed information. If possible, heating the sample to even higher temperatures might also provide

insight whether we are already working with clean or only less contaminated samples.

For future studies concerning suspended 2D materials I strongly suggest using cleaned samples. Measurements using single layer graphene as a sample haven shown that cleaning is necessary to measure the properties of the true two-dimensional material itself and avoid artifacts from contaminations. The tools for this were installed and demonstrated in this thesis.

Danksagung

Als ich vor etwas mehr als zweieinhalb Jahren für Arbeiten im Zuge meiner Bachelorarbeit ein Teil der Arbeitsgruppe für Atom- und Plasmaphysik wurde, wusste ich schnell, dass ich mein wissenschaftliches Zuhause gefunden hatte. Auch heute freue ich mich noch auf jeden Tag, den ich bei Diskussionen über Physik, ausgiebigen Kaffee- und Mittagspausen und sogar bei langen Gruppenbesprechungen gemeinsam mit euch verbringen darf. Zum Ende meines Masterstudiums bietet sich nun einmal die Gelegenheit, mich bei all jenen zu bedanken, die diese Zeit zu einer besonderen gemacht haben.

Der größte Dank gebührt dir, lieber *Fritz*. Wie du diese Arbeitsgruppe neben all deinen anderen Verpflichtungen leitest, jederzeit ein offenes Ohr, gute Ideen und aufmunternde Worte für uns hast, ist bemerkenswert - dass du es darüber hinaus mit einem unglaublichen Gespür schaffst, stets nicht nur eine Arbeitsgruppe, sondern viel mehr eine kleine Familie hier zu versammeln, wahrlich beeindruckend. Ich danke dir für alle Erfahrungen, die ich in den letzten Jahren mit deiner Unterstützung in der Welt der Wissenschaft sammeln durfte: vor allem die Aufenthalte in Uppsala sowie die Konferenzteilnahmen in Frankreich möchte ich dabei hervorheben.

Lieber *Richard*, auch bei dir möchte ich mich herzlich für deine fortwährende Unterstützung bedanken, ohne die es meine Arbeit in dieser Form nicht gäbe. Sowohl mit deinem Wissen, das mich immer wieder aufs Neue beeindruckt, als auch mit Gesprächen über Feinheiten in Texten und vor allem Graphiken (und der Einführung in DataGraph) hast du diese Arbeit geprägt. Deine Fähigkeit, in kürzester Zeit Lösungsansätze für jegliche Probleme zu entwickeln, ist imponierend und auch das macht es zu einem Vergnügen, von dir zu lernen.

Ich schätze eure Unterstützung sehr und freue mich schon darauf, auch in den kommenden Jahren weitere wissenschaftliche Erfahrungen an eurer Seite zu sammeln!

Zu einem großen Teil ist es auch dir, liebe *Janine*, zu verdanken, dass wir nun diese Arbeit lesen können. Du hast mich in die Welt der Wissenschaft und unseres Labors eingeführt und dabei geholfen, die Begeisterung für unsere Forschung zu wecken. Dass ich auch nach meiner Bachelorarbeit mit all meinen Fragen und Problemen - egal ob wissenschaftlich oder nicht - zu dir kommen konnte und du dir immer Zeit für mich genommen hast, bedeutet mir viel.

Selbstverständlich gebührt auch allen anderen, die diese Arbeitsgruppe zu der machen, die sie ist, ein großes Dankeschön: dafür, dass du es mit deiner Ruhe immer schaffst mich vor Verzweiflungen zu bewahren und jederzeit bereit bist mitzudenken, wenn einmal ein Knoten in

meinem Kopf zu lösen ist, *Paul*; dafür, dass du, *Reinhard*, mir immer zur Seite stehst, wenn ich vor neuen Herausforderungen im Labor stehe; dafür, dass du mich mit deiner Fröhlichkeit auch an Tagen, an denen im Labor nichts funktioniert, zum Lachen bringst, *Georg*; dafür, dass du, *Herbert*, mir oft die Zeit im Büro mit Schlagern des Tages und Elektronikrätseln aufgelockert hast.

Auch ihr, *Christian*, *Daniel*, *Gabriel*, *Ille*, *Lidija*, *Martin* und *Sascha*, habt die Zeit meiner Diplomarbeit mit hilfreichen Diskussionen und auflockernden Gesprächen geprägt, genauso wie *Benjamin* und *Raphael* und viele weitere, die ich in dieser Zeit als Kollegen und Kolleginnen kennen und schätzen lernen durfte.

Da dies nicht nur das Ende meiner Diplomarbeit, sondern auch das Ende meiner Studienzeit mit meiner Lerngruppe bedeutet, sei auch dieser ein Dankeschön für die vergangenen fünf Jahre ausgesprochen. Besonders gemeinsam mit dir, *Martin*, habe ich durch das Rechnen unserer Übungen, unsere mitternächtlichen Skype-Calls und dem gemeinsamen Lernen für fast alle Prüfungen im Bachelor viel erreicht. Es waren große Fußstapfen, die zu füllen waren, nachdem wir im Master getrennte Wege gegangen sind, doch du, *Manuel*, warst mir in diesem Abschnitt ein ebenso guter Kumpan. Zu den "(Joh)annas" gehörten neben euch beiden auch Johanna, Daniel und du, *Johanna* - es war mir eine Freude, dich jetzt auch als Kollegin in der AG begrüßen zu dürfen. Dir danke ich auch besonders, genauso wie auch dir, *Paul*, dafür, dass ihr euch durch diese Arbeit gekämpft und sie auf Korrekturen durchgelesen habt.

Das Verfassen von Arbeiten wird mich auch immer an dich erinnern, lieber *Gerhard*. Mir hätte in meiner Ausbildung nichts Besseres passieren können, als dass du uns (leider erst) in der 6. Klasse in Mathematik übernommen hast. Du hast mich nicht nur die Geheimnisse (und viele Tricks) der Mathematik, das Verfassen wissenschaftlicher Arbeiten und die richtigen Ansichten und das Zeichnen von Modellen gelehrt - viel wichtiger, du hast mir deine Faszination für und Begeisterung an der Wissenschaft weitergegeben, mit denen mich meine Kollegen auf der Uni kennenlernen durften, und ohne die ich es nicht mit dieser Freude soweit geschafft hätte. Vielen Dank für deine Förderung und all die Zeit, die du dir für mich und meine FBA genommen hast.

Last but not least möchte ich mich bei meiner Familie, allen voran bei meinen Eltern, *Susanne* und *Albert*, bedanken, dafür, dass ihr immer hinter mir steht und ich immer auf eure Unterstützung zählen kann.

Bibliography

[1] J. Baglin, "Ion beam nanoscale fabrication and lithography - A review," *Applied Surface Science*, vol. 258, p. 4103, 2012.

[2] J. Mayer, "Ion implantation in semiconductors," in *1973 International Electron Devices Meeting*, p. 3, IRE, 1973.

[3] J. Perrière, "Rutherford backscattering spectrometry," *Vacuum*, vol. 37, p. 429, 1987.

[4] W. Arnold Bik and F. Habraken, "Elastic recoil detection," *Reports on Progress in Physics*, vol. 56, p. 859, 1993.

[5] W. Chu, J. Mayer, M. Nicolet, T. Buck, G. Amsel, and F. Eisen, "Principles and applications of ion beam techniques for the analysis of solids and thin films," *Thin Solid Films*, vol. 17, p. 1, 1973.

[6] D. Fink and L. Chadderton, "Ion-solid interactions: current status, new perspectives," *Radiation Effects & Defects in Solids*, vol. 160, p. 67, 2005.

[7] J. Arianer and R. Geller, "The advanced positive heavy ion sources," *Annu. Rev. Nucl. Part. Sci.*, vol. 31, p. 19, 1981.

[8] R. Geller, "ECRIS: The Electron Cyclotron Resonance Ion Sources," *Annu. Rev. Nucl. Part. Sci.*, vol. 40, p. 15, 1990.

[9] F. Aumayr, S. Facsko, A. El-Said, C. Trautmann, and M. Schleberger, "Single ion induced surface nanostructures: a comparison between slow highly charged and swift heavy ions," *Journal of Physics: Condensed Matter*, vol. 23, p. 393001, 2011.

[10] E. Gruber, P. Salou, L. Bergen, M. El Kharrazi, E. Lattouf, C. Grygiel, Y. Wang, A. Benyagoub, D. Levavasseur, J. Rangama, H. Lebius, B. Ban-d'Etat, M. Schleberger, and F. Aumayr, "Swift heavy ion irradiation of CaF_2 – from grooves to hillocks in a single ion track," *Journal of Physics: Condensed Matter*, vol. 28, p. 405001, 2016.

[11] M. Toulemonde, W. Assmann, C. Trautmann, F. Grüner, H. Mieskes, H. Kucal, and Z. Wang, "Electronic sputtering of metals and insulators by swift heavy ions," *Nuclear Instruments and*

Methods in Physics Research, Section B: Beam Interactions with Materials and Atoms, vol. 212, p. 346, 2003.

[12] W. Assmann, M. Toulemonde, and C. Trautmann, "Electronic Sputtering with Swift Heavy Ions," in *Sputtering by Particle Bombardment*, p. 401, Springer Berlin Heidelberg, 2007.

[13] R. Honig, "Sputtering of Surfaces by Positive Ion Beams of Low Energy," *Journal of Applied Physics*, vol. 29, p. 2345, 1958.

[14] H. Winter, "Kinetic Electron Emission for Grazing Scattering of Atoms and Ions from Surfaces," in *Slow Heavy-Particle Induced Electron Emission from Solid Surfaces*, p. 113, Springer Berlin Heidelberg, 2007.

[15] F. Aumayr, A. El-Said, and W. Meissl, "Nano-sized surface modifications induced by the impact of slow highly charged ions - A first review," *Nuclear Instruments and Methods in Physics Research, Section B: Beam Interactions with Materials and Atoms*, vol. 266, p. 2729, 2008.

[16] F. Aumayr and H. Winter, "Potential sputtering," *Philosophical Transactions of the Royal Society of London A: Mathematical, Physical and Engineering Sciences*, vol. 362, p. 77, 2004.

[17] G. Hayderer, S. Cernusca, M. Schmid, P. Varga, H. Winter, F. Aumayr, D. Niemann, V. Hoffmann, N. Stolterfoht, C. Lemell, L. Wirtz, and J. Burgdörfer, "Kinetically Assisted Potential Sputtering of Insulators by Highly Charged Ions," *Physical Review Letters*, vol. 86, p. 3530, 2001.

[18] F. Aumayr and H. Winter, "Potential Electron Emission from Metal and Insulator Surfaces," in *Slow Heavy-Particle Induced Electron Emission from Solid Surfaces*, p. 79, Springer Berlin Heidelberg, 2007.

[19] E. Gruber, *Interaction of ions with 2D and 3D materials*. PhD thesis, TU Wien, 2017.

[20] F. Aumayr, H. Kurz, D. Schneider, M. Briere, W. Mcdonald, C. Cunningham, and H. Winter, "Emission of Electrons from a Clean Gold Surface Induced by Slow, Very Highly Charged Ions at the Image Charge Acceleration Limit," *Physical Review Letters*, vol. 71, p. 1943, 1993.

[21] M. Simon, "Elektronen-Emission bei Beschuss von Isolator- und Metall-Oberflächen mit hochgeladenen Ionen," diploma thesis, TU Wien.

[22] H. Winter, M. Vana, C. Lemell, and F. Aumayr, "Interaction of slow multicharged ions with solid surfaces: current concepts and new information on slow electron emission," *Nuclear*

Instruments and Methods in Physics Research Section B: Beam Interactions with Materials and Atoms, vol. 115, p. 224, 1996.

[23] J. Schwestka, A. Niggas, S. Creutzburg, R. Kozubek, R. Heller, M. Schleberger, R. Wilhelm, and F. Aumayr, "Charge-Exchange-Driven Low-Energy Electron Splash Induced by Heavy Ion Impact on Condensed Matter," *The Journal of Physical Chemistry Letters*, vol. 10, p. 4805, 2019.

[24] J. Burgdörfer, P. Lerner, and F. Meyer, "Above-surface neutralization of highly charged ions: The classical over-the-barrier model," *Physical Review A*, vol. 44, p. 5674, 1991.

[25] J. Briand, L. de Billy, P. Charles, S. Essabaa, P. Briand, R. Geller, J. Desclaux, S. Bliman, and C. Ristori, "Production of hollow atoms by the excitation of highly charged ions in interaction with a metallic surface," *Physical Review Letters*, vol. 65, p. 159, 1990.

[26] H. Winter and F. Aumayr, "Hollow atoms," *Journal of Physics B: Atomic, Molecular and Optical Physics*, vol. 32, p. R39, 1999.

[27] A. Arnau, F. Aumayr, P. Echenique, M. Grether, W. Heiland, J. Limburg, R. Morgenstern, P. Roncin, S. Schippers, R. Schuch, N. Stolterfoht, P. Varga, T. Zouros, and H. Winter, "Interaction of slow multicharged ions with solid surfaces," *Surface Science Reports*, vol. 27, p. 113, 1997.

[28] R. Wilhelm, E. Gruber, J. Schwestka, R. Kozubek, T. Madeira, J. Marques, J. Kobus, A. Krasheninnikov, M. Schleberger, and F. Aumayr, "Interatomic Coulombic Decay: The Mechanism for Rapid Deexcitation of Hollow Atoms," *Physical Review Letters*, vol. 119, p. 103401, 2017.

[29] L. Cederbaum, J. Zobeley, and F. Tarantelli, "Giant Intermolecular Decay and Fragmentation of Clusters," *Physical Review Letters*, vol. 79, p. 4778, 1997.

[30] T. Jahnke, A. Czasch, M. Schöffler, S. Schössler, A. Knapp, M. Käsz, J. Titze, C. Wimmer, K. Kreidi, R. Grisenti, A. Staudte, O. Jagutzki, U. Hergenhahn, H. Schmidt-Böcking, and R. Dörner, "Experimental Observation of Interatomic Coulombic Decay in Neon Dimers," *Physical Review Letters*, vol. 93, p. 163401, 2004.

[31] T. Jahnke, "Interatomic and intermolecular Coulombic decay: the coming of age story," *Journal of Physics B: Atomic, Molecular and Optical Physics*, vol. 48, p. 082001, 2015.

[32] R. Wilhelm, E. Gruber, J. Schwestka, R. Heller, S. Fascko, and F. Aumayr, "Neutralization Dynamics of Slow Highly Charged Ions in 2D Materials," *Applied Sciences*, vol. 8, p. 1050, 2018.

[33] J. Schwestka, R. Wilhelm, E. Gruber, R. Heller, R. Kozubek, M. Schleberger, S. Facsko, and F. Aumayr, "The role of radiative de-excitation in the neutralization process of highly charged ions interacting with a single layer of graphene," *Nuclear Instruments and Methods in Physics Research Section B: Beam Interactions with Materials and Atoms*, vol. 422, p. 63, 2018.

[34] R. Wilhelm and P. Grande, "Unraveling energy loss processes of low energy heavy ions in 2D materials," *Communications Physics*, vol. 2, p. 89, 2019.

[35] Royal Swedish Academy of Sciences, "Nobel prize 2010," *https://www.nobelprize.org/prizes/physics/2010/press-release/*, 2019 (accessed October 10, 2019).

[36] K. Novoselov, A. Geim, S. Morozov, D. Jiang, Y. Zhang, S. Dubonos, I. Grigorieva, and A. Firsov, "Electric Field Effect in Atomically Thin Carbon Films," *Science*, vol. 306, p. 666, 2004.

[37] K. Novoselov, D. Jiang, F. Schedin, T. Booth, V. Khotkevich, S. Morozov, and A. Geim, "Two-dimensional atomic crystals," *PNAS*, vol. 102, p. 10451, 2005.

[38] K. Novoselov, A. Mishchenko, A. Carvalho, and A. Castro Neto, "2D materials and van der Waals heterostructures," *Science*, vol. 353, p. 461, 2016.

[39] A. Geim and I. Grigorieva, "Van der Waals heterostructures," *Nature*, vol. 499, p. 419, 2013.

[40] F. Withers, O. Del Pozo-Zamudio, A. Mishchenko, A. Rooney, A. Gholinia, K. Watanabe, T. Taniguchi, S. Haigh, A. Geim, A. Tartakovskii, and K. Novoselov, "Light-emitting diodes by band-structure engineering in van der Waals heterostructures," *Nature Materials*, vol. 14, p. 301, 2015.

[41] L. Wang, I. Meric, P. Huang, Q. Gao, Y. Gao, H. Tran, T. Taniguchi, K. Watanabe, L. Campos, D. Muller, J. Guo, P. Kim, J. Hone, K. Shepard, and C. Dean, "One-dimensional electrical contact to a two-dimensional material.," *Science*, vol. 342, p. 614, 2013.

[42] X. Wang and F. Xia, "Stacked 2D materials shed light," *Nature Materials*, vol. 14, p. 264, 2015.

[43] J. Ross, S. Wu, H. Yu, N. Ghimire, A. Jones, G. Aivazian, J. Yan, D. Mandrus, D. Xiao, W. Yao, and X. Xu, "Electrical control of neutral and charged excitons in a monolayer semiconductor," *Nature Communications*, vol. 4, p. 2498, 2013.

[44] J. Abraham, K. Vasu, C. Williams, K. Gopinadhan, Y. Su, C. Cherian, J. Dix, E. Prestat, S. Haigh, I. Grigorieva, P. Carbone, A. Geim, and R. Nair, "Tunable sieving of ions using graphene oxide membranes," *Nature Nanotechnology*, vol. 12, p. 546, 2017.

[45] R. Nair, H. Wu, P. Jayaram, I. Grigorieva, and A. Geim, "Unimpeded Permeation of Water Through Helium-Leak-Tight Graphene-Based Membranes," *Science*, vol. 335, p. 442, 2012.

[46] R. En Mas-Ballest, C. Omez-Navarro, J. Omez-Herrero, and F. Elix Zamora, "2D materials: to graphene and beyond," *Nanoscale*, vol. 3, p. 20, 2011.

[47] A. Geim and K. Novoselov, "The rise of graphene," *Nature Materials*, vol. 6, p. 183, 2007.

[48] Y. Huang, J. Wu, and K. Hwang, "Thickness of graphene and single-wall carbon nanotubes," *Physical Review B*, vol. 74, p. 245413, 2006.

[49] E. Duplock, M. Scheffler, and P. Lindan, "Hallmark of Perfect Graphene," *Physical Review Letters*, vol. 92, p. 225502, 2004.

[50] A. Castro Neto, F. Guinea, N. Peres, K. Novoselov, and A. Geim, "The electronic properties of graphene," *Reviews of Modern Physics*, vol. 81, p. 109, 2009.

[51] Graphenea, "Graphene on TEM grids," *https://www.graphenea.com*, 2019 (accessed October 13, 2019).

[52] H. Chen, J. Huang, X. Lei, M. Wu, G. Liu, C. Ouyang, and B. Xu, "Adsorption and Diffusion of Lithium on MoS_2 Monolayer: The Role of Strain and Concentration," *International Journal of Electrochemical Science*, vol. 8, p. 2196, 2013.

[53] O. Ochedowski, K. Marinov, N. Scheuschner, A. Poloczek, B. Bussmann, J. Maultzsch, M. Schleberger, U. Schwarz, and M. Baykara, "Effect of contaminations and surface preparation on the work function of single layer MoS 2," *Beilstein Journal of Nanotechnology*, vol. 5, p. 291, 2014.

[54] P. Zhao, A. Kumamoto, S. Kim, X. Chen, B. Hou, S. Chiashi, E. Einarsson, Y. Ikuhara, and S. Maruyama, "Self-Limiting Chemical Vapor Deposition Growth of Monolayer Graphene from Ethanol," *The Journal of Physical Chemistry C*, vol. 117, p. 10755, 2013.

[55] J. Suk, A. Kitt, C. Magnuson, Y. Hao, S. Ahmed, J. An, A. Swan, B. Goldberg, and R. Ruoff, "Transfer of CVD-Grown Monolayer Graphene onto Arbitrary Substrates," *ACS Nano*, vol. 5, p. 6916, 2011.

[56] F. Bonaccorso, A. Lombardo, T. Hasan, Z. Sun, L. Colombo, and A. Ferrari, "Production and processing of graphene and 2d crystals," *Materials Today*, vol. 15, p. 564, 2012.

[57] Y.-C. Lin, C.-C. Lu, C.-H. Yeh, C. Jin, K. Suenaga, and P.-W. Chiu, "Graphene Annealing: How Clean Can It Be?," *Nano Letters*, vol. 12, p. 414, 2012.

[58] W. Van Dorp, X. Zhang, B. Feringa, J. Wagner, T. Hansen, J. Th, and M. De Hosson, "Nanometer-scale lithography on microscopically clean graphene," *Nanotechnology*, vol. 22, p. 505303, 2011.

[59] G. Algara-Siller, O. Lehtinen, A. Turchanin, and U. Kaiser, "Dry-cleaning of graphene," *Applied Physics Letters*, vol. 104, p. 153115, 2014.

[60] G. Lupina, J. Kitzmann, I. Costina, M. Lukosius, C. Wenger, A. Wolff, S. Vaziri, M. Stling, I. Pasternak, A. Krajewska, W. Strupinski, S. Kataria, A. Gahoi, M. Lemme, G. Ruhl, G. Zoth, O. Luxenhofer, and W. Mehr, "Residual Metallic Contamination of Transferred Chemical Vapor Deposited Graphene," *Nano*, vol. 9, p. 4776, 2015.

[61] E. Gruber, R. Wilhelm, R. Pétuya, V. Smejkal, R. Kozubek, A. Hierzenberger, B. Bayer, I. Aldazabal, A. Kazansky, F. Libisch, A. Krasheninnikov, M. Schleberger, S. Facsko, A. Borisov, A. Arnau, and F. Aumayr, "Ultrafast electronic response of graphene to a strong and localized electric field," *Nature Communications*, vol. 7, p. 13948, 2016.

[62] A. Kretinin, Y. Cao, J. Tu, G. Yu, R. Jalil, K. Novoselov, S. Haigh, A. Gholinia, A. Mishchenko, M. Lozada, T. Georgiou, C. Woods, F. Withers, P. Blake, G. Eda, A. Wirsig, C. Hucho, K. Watanabe, T. Taniguchi, A. Geim, and R. Gorbachev, "Electronic Properties of Graphene Encapsulated with Different Two-Dimensional Atomic Crystals," *Nano Letters*, vol. 14, p. 3270, 2014.

[63] R. Zan, Q. Ramasse, U. Bangert, and K. Novoselov, "Graphene Reknits Its Holes," *Nano Letters*, vol. 12, p. 5, 2012.

[64] H. Nan, Z. Ni, J. Wang, Z. Zafar, Z. Shi, and Y. Wang, "The thermal stability of graphene in air investigated by Raman spectroscopy," *Journal of Raman Spectroscopy*, vol. 44, p. 1018, 2013.

[65] Z. Ni, H. Wang, Z. Luo, Y. Wang, T. Yu, Y. Wu, and Z. Shen, "The effect of vacuum annealing on graphene," *Journal of Raman Spectroscopy*, vol. 41, p. 479, 2009.

[66] K. Kim, W. Regan, B. Geng, B. Alemán, B. Kessler, F. Wang, M. Crommie, and A. Zettl, "High-temperature stability of suspended single-layer graphene," *Physica Status Solidi - Rapid Research Letters*, vol. 4, p. 302, 2010.

[67] M. Tripathi, A. Mittelberger, K. Mustonen, C. Mangler, J. Kotakoski, J. Meyer, and T. Susi, "Cleaning graphene: Comparing heat treatments in air and in vacuum," *Physica Status Solidi - Rapid Research Letters*, vol. 11, p. 1700124, 2017.

[68] A. Pirkle, J. Chan, A. Venugopal, D. Hinojos, C. Magnuson, S. Mcdonnell, L. Colombo, E. Vogel, R. Ruoff, and R. Wallace, "The effect of chemical residues on the physical and electrical properties of chemical vapor deposited graphene transferred to SiO_2," *Applied Physics Letters*, vol. 99, p. 122108, 2011.

[69] J. Wang, Z. Chen, and B. Chen, "Adsorption of Polycyclic Aromatic Hydrocarbons by Graphene and Graphene Oxide Nanosheets," *Environmental Science & Technology*, vol. 48, p. 4817, 2014.

[70] J. Moser, A. Barreiro, and A. Bachtold, "Current-induced cleaning of graphene," *Applied Physics Letters*, vol. 91, p. 163513, 2007.

[71] M. Schleberger and J. Kotakoski, "2D Material Science: Defect Engineering by Particle Irradiation," *Materials*, vol. 11, p. 1885, 2018.

[72] R. Kozubek, M. Tripathi, M. Ghorbani-Asl, S. Kretschmer, L. Madauß, E. Pollmann, M. O'Brien, N. McEvoy, U. Ludacka, T. Susi, G. Duesberg, R. Wilhelm, A. Krasheninnikov, J. Kotakoski, and M. Schleberger, "Perforating Freestanding Molybdenum Disulfide Monolayers with Highly Charged Ions," *The Journal of Physical Chemistry Letters*, vol. 10, p. 904, 2019.

[73] G. Zschornack, M. Kreller, V. Ovsyannikov, F. Grossman, U. Kentsch, M. Schmidt, F. Ullmann, and R. Heller, "Compact electron beam ion sources/traps: Review and prospects (invited)," *Review of Scientific Instruments*, vol. 79, p. 02A703, 2008.

[74] U. Kentsch, S. Landgraf, G. Zschornack, F. Grossmann, V. Ovsyannikov, and F. Ullmann, "Dresden EBIT: Results and perspectives," *Review of Scientific Instruments*, vol. 73, p. 660, 2002.

[75] DREEBIT, "Dresden EBIS-A - DREEBIT | Ion Beam Technology," *http://www.dreebit-ibt.com/product/dresden-ebis-a.html*, 2019 (accessed May 27, 2019).

[76] J. Schwestka, D. Melinc, R. Heller, A. Niggas, L. Leonhartsberger, H. Winter, S. Facsko, F. Aumayr, and R. Wilhelm, "A versatile ion beam spectrometer for studies of ion interaction with 2D materials," *Review of Scientific Instruments*, vol. 89, p. 085101, 2018.

[77] EM Resolutions, "Formvar/Carbon film on Copper 300 mesh (50) - EM Resolutions," *https://emresolutions.com/product/formvarcarbon-film-on-copper-300-mesh-50/*, 2019 (accessed June 29, 2019).

[78] Lasertack GmbH, "Lasertack - New Laser Generation. NUBM44," *https://www.lasertack.com/6w-445nm-laserdiodenmodul-nubm44*, 2019 (accessed August 10, 2019).

[79] H. Kurz, F. Aumayr, H. Winter, D. Schneider, M. Briere, and J. Mcdonald, "Electron emission and image-charge acceleration for the impact of very highly charged ions on clean gold," *Physical Review A*, vol. 49, p. 4693, 1994.

[80] T. Kalvas, O. Tarvainen, T. Ropponen, O. Steczkiewicz, J. Ärje, and H. Clark, "IBSIMU: A three-dimensional simulation software for charged particle optics a…," *Review of Scientific Instruments*, vol. 81, p. 02B703, 2010.

[81] RoentDek Handels GmbH, "CoboldPC Software," *http://www.roentdek.com/*, 2018 (accessed August 22, 2019).

[82] J. Ziegler, M. Ziegler, and J. Biersack, "SRIM - The stopping and range of ions in matter (2010)," *Nuclear Instruments and Methods in Physics Research, Section B: Beam Interactions with Materials and Atoms*, vol. 268, p. 1818, 2010.